

1 **EVALUATION OF AN EXTREME-CONDITION-INVERSE CALIBRATION**
2 **REMOTE SENSING MODEL FOR MAPPING ENERGY BALANCE FLUXES IN**
3 **ARID RIPARIAN AREAS**

4
5 Sung-ho Hong¹, Jan M.H. Hendrickx^{2*}, Jan Kleissl³, Rick G. Allen⁴,
6 Wim G.M. Bastiaanssen⁵, Russell L. Scott⁶, Aaron L. Steinwand⁷
7

8 ¹Murray State University, Murray, KY; previously, New Mexico Tech, Socorro, NM; ²New
9 Mexico Tech, Socorro, NM; ³University of California, San Diego, CA; ⁴University of Idaho,
10 Kimberly, ID; ⁵Delft University of Technology and UNESCO-IHE, Delft, The Netherlands;
11 ⁶Southwest Watershed Research Center, USDA-ARS, Tucson, AZ; ⁷Inyo County, Water
12 Department, Independence, CA.

13
14 **ABSTRACT**

15 Accurate information on the distribution of the surface energy balance components in
16 arid riparian areas is needed for sustainable management of water resources as well as for
17 developing a better understanding of water and heat exchange processes between the land
18 surface and atmosphere. Since the spatial and temporal distributions of these fluxes over large
19 areas are difficult to determine from ground measurements, their prediction from remote sensing
20 data is very attractive due to its large areal coverage and a high repetition rate. In this study the
21 Surface Energy Balance Algorithm for Land (SEBAL) was used as a remote-sensing platform to
22 estimate energy balance components in the arid riparian areas of the Middle Rio Grande Basin
23 (New Mexico) and San Pedro Basin (Arizona), and areas of phreatophytic shrubs and grasses in
24 the Owens Valley (California). We compared instantaneous and daily fluxes from SEBAL
25 derived from Landsat TM images to surface-based measurements from eddy covariance flux
26 towers. This study presents evidence that inversion-calibrated surface energy balance models

* Corresponding author: janhendrickxnmt@gmail.com

Deleted: Bishop

Deleted: ¶

Formatted: Font: Not Bold

Formatted: Left, Line spacing: single, Widow/Orphan control

Deleted: the

Deleted: alone

Deleted: as it enables

Deleted: area

Deleted: all the

Deleted:),

Deleted: compare

Deleted: SEBAL

Deleted: with

Formatted: Indent: Left: 0"

38 such as SEBAL and similar models such as METRIC can yield reliable estimates for actual
39 evapotranspiration rates in riparian areas of the southwestern United States. The great strengths
40 of the inversion-calibrated methods are their internal calibration strategies that eliminate much of
41 the effects of systematic biases in net radiation, soil heat flux, land surface temperature and
42 albedo on latent heat flux, at the expense of increased bias in sensible heat flux.

Deleted: yields

Deleted: strength

Deleted: SEBAL method is its

Deleted: procedure

Deleted: eliminates most

Deleted: bias

44 1. INTRODUCTION

45 The regional distribution of the energy balance components, net surface radiation (R_n),
46 soil heat flux (G), sensible heat flux (H) and latent heat flux (LE) in arid riparian areas is critical
47 knowledge for agricultural, hydrological and climatological investigations. However, R_n , G , H
48 and LE are complex functions of atmospheric conditions, land use, vegetation, soils, and
49 topography which cause these fluxes to vary in space and time. It is difficult or impractical to
50 estimate surface fluxes at the regional scale using ground-based instruments (Parlange et al.,
51 1995). Measurement approaches for LE from the land surface such as eddy covariance (Kizer
52 and Elliott, 1991), Bowen ratio (Scott et al., 2004) and weighing lysimeters (Wright, 1982) are
53 too expensive and time consuming for continuous application at sufficient spatial density at
54 regional scales. These techniques produce LE measurements over small footprints (m^2 to ha)
55 which are difficult to extrapolate to the regional scale, especially over heterogeneous land
56 surfaces (Moran and Jackson, 1991). For example, in the heterogeneous landscape of the central
57 plateau of Spain as many as 13 ground measurements of evapotranspiration in a relatively small
58 area of 5000 km^2 were not sufficient to predict accurately the area-averaged evapotranspiration
59 rate (Pelgrum and Bastiaanssen, 1996).

Deleted: Therefore, it is difficult to estimate them at the regional scale (Parlange et al., 1995). Measurement approaches for LE from the land surface including eddy covariance (Kizer and Elliott, 1991), Bowen ratio (Scott et al., 2004) and weighing lysimeters (Wright, 1982) are too expensive and time consuming for continuous application at sufficient spatial density at the regional scale. These techniques produce LE measurements over small footprints (m^2 to ha) which are difficult to extrapolate to the regional scale, especially over heterogeneous land surfaces (Moran and Jackson, 1991). For example, in the heterogeneous landscape of the central plateau of Spain as many as 13 ground measurements of evapotranspiration in a relatively small area of 5000 km^2 were not sufficient to predict accurately the area-averaged evapotranspiration rate (Pelgrum and Bastiaanssen, 1996).

80 A number of studies have concluded that reliable regional estimates of spatial patterns of
 81 LE can be obtained by satellite image-based remote sensing algorithms (e.g. Choudhury,
 82 1989;Granger, 2000;Moran and Jackson, 1991;Kustas and Norman, 1996;Du et al., 2013). A
 83 variety of LE remote sensing algorithms exists with different spatial (30 m to 1/8th degree or 13
 84 km in New Mexico) and temporal (daily to monthly) scales. Examples include: the Two-Source
 85 Energy Balance model (TSEB) (Norman et al., 1995), the Hybrid dual source Trapezoid
 86 framework Evapotranspiration Model (HTEM) (Yang and Shang, 2013), the Atmosphere-Land
 87 Exchange Inverse (ALEXI) (Anderson et al., 1997), the disaggregated ALEXI model (DisALEXI)
 88 (Norman et al., 2003), the Surface Energy Balance System (SEBS) (Su, 2002), the MOD16 ET
 89 algorithms (Mu et al., 2011), the Simplified Surface Energy Balance (SSEB) (Senay et al., 2013),
 90 the Surface Energy Balance Algorithm for Land (SEBAL) (Bastiaanssen, 1995), Mapping
 91 EvapoTranspiration at high spatial Resolution with Internalized Calibration (METRIC) (Allen et
 92 al., 2007), as well as algorithms without distinct acronyms (Schüttemeyer et al., 2007;Ma et al.,
 93 2004;Jiang and Islam, 2001).

Deleted: Reliable

Deleted: only

Deleted: as has been shown by a number of investigators

Deleted: . Today a variety of *LE* remote sensing algorithms exists with different spatial (30 m to 1/8th degree or 13 km in New Mexico) and temporal (daily to monthly) scales: the North American Land Data Assimilation Systems (NLDAS) (Cosgrove et al., 2003), the Land Information Systems (LIS) (Peters Lidard et al., 2004), the Two-Source Energy Balance model (TSEB) (Norman et al., 1995), the Hybrid dual source Trapezoid framework Evapotranspiration Model (HTEM) (Yang and Shang, 2013), the Atmosphere-Land Exchange Inverse (ALEXI) (Anderson et al., 1997), the disaggregated ALEXI model (DisALEXI) (Norman et al., 2003), the Surface Energy Balance System (SEBS) (Su, 2002), the MOD16 ET algorithms (Mu et al., 2011), the Simplified Surface Energy Balance (SSEB) (Senay et al., 2013), the Surface Energy Balance Algorithm for Land (SEBAL) (Bastiaanssen, 1995), Mapping EvapoTranspiration at high spatial Resolution with Internalized Calibration (METRIC) (Allen et al., 2007), as well as algorithms without distinct acronyms (Schüttemeyer et al., 2007;Ma et al., 2004;Jiang and Islam, 2001). ¶ SEBAL has been developed and pioneered by Bastiaanssen and his colleagues in The Netherlands during the 1990s (Bastiaanssen, 1995). METRIC has been developed by Allen and his research team in Idaho using SEBAL as its foundation (Allen et al., 2005). Unlike ALEXI and DisALEXI, SEBAL and METRIC do not require spatial fields of air temperature and atmospheric temperature soundings interpolated across the region of interest; unlike NLDAS and LIS, SEBAL and METRIC do not require land cover maps. However, applications of SEBAL and METRIC are restricted to clear days over areas of unvarying weather, and require some supervised calibration for each image, preventing application at the continental scale such as done by ALEXI, SSEB, MOD16, NLDAS and LIS.¶

Deleted:

Deleted: (Allen et al., 2007b)

94 SEBAL was developed by Bastiaanssen and his colleagues in The Netherlands during
 95 the 1990s (Bastiaanssen, 1995). METRIC was developed by Allen and his research team in Idaho
 96 using SEBAL as its foundation (Allen et al., 2005), but with greater reliance on weather-based
 97 reference ET calculations for calibration. SEBAL and METRIC do not require spatial fields of
 98 air temperature and atmospheric temperature soundings interpolated across the region of interest
 99 like ALEXI and DisALEXI. SEBAL and METRIC do not require land cover maps for estimating
 100 surface roughness but instead can use expressions that relate the NDVI to the momentum
 101 roughness length (Bastiaanssen et al., 1998a;Allen et al., 2007). However, SEBAL and METRIC

137 are restricted to clear days over areas of stable weather and generally require some supervised
138 calibration for each image. These requirements limit their application to local and regional scale,
139 rather than at continental scale that is possible with ALEXI, SSEB, or MOD16. Interpolation of
140 ET between images is done using ground-based or gridded reference ET and interpolated
141 fractions of reference ET.

142 The accuracy of SEBAL and METRIC for evaporation mapping worldwide is typically
143 about $\pm 15\%$ for daily and $\pm 1-5\%$ for seasonal evaporation estimates (Bastiaanssen et al.,
144 2005; Allen et al., 2011; Karimi and Bastiaanssen, 2015). Accuracy of the models depends on a
145 calibration method that selects a “cold” and “hot” pixel representing extreme thermal and
146 vegetation conditions within an image. After calculation of the energy balance at the two
147 calibration pixels, the near-surface air temperature gradient associated with sensible heat flux H
148 for each pixel is indexed to its satellite measured surface temperature.

149 The economic efficiency of SEBAL and METRIC is particularly attractive. For example,
150 in the early 1980's co-author Hendrickx with a team of field assistants and graduate students
151 spent two years in the Office du Niger (Mali) to measure the seasonal actual evapotranspiration
152 of rice in four irrigation units encompassing an area of about 70 hectares using non-weighing
153 lysimeters and discharge measurements in irrigation and drainage ditches (Hendrickx et al.,
154 1986). For comparison, in 2008, the seasonal actual evapotranspiration was obtained by two
155 scientists, (Zwart and Leclert, 2010), for 86,000 hectares from the Office du Niger using SEBAL
156 with Landsat imagery of 2006 in approximately two months. The economy of the method
157 justifies further investigations to validate the SEBAL model for a variety of field environments.

Deleted: and $\pm 5\%$

Deleted: , respectively,

Deleted: (Bastiaanssen et al., 2005; Allen et al., 2011). Such accuracy is obtained by

Deleted: the

Deleted: remarkable.

Deleted: was deployed at Niono

Deleted: in

Deleted: to determine water requirements for flood irrigated rice. It took him and a team of four field assistants and several graduate students more than two years

Deleted: covering a total

Deleted: measurement structures

Deleted: (Hendrickx et al., 1986). In

Deleted: for all

Deleted: of

Deleted: at an effort of about

Deleted: expert

Deleted: without need for an overseas multi-year deployment (Zwart and Leclert, 2010).

178 Previous validation studies of SEBAL have been conducted in relatively homogeneous
 179 agricultural areas and have focused on a comparison of daily ET rates estimated from SEBAL (or
 180 METRIC) with ground measurements using lysimeters (Tasumi, 2003;Trezza, 2002). Bowen
 181 ratio and eddy covariance methods (Gibson et al., 2013;Du et al., 2013;Bastiaanssen et al., 2002)
 182 and scintillometry (Hemakumara et al., 2003;Kite and Droogers, 2000;Kleissl et al., 2009). The
 183 overall goal of this study was to conduct a thorough evaluation of the performance of SEBAL in
 184 arid riparian areas in New Mexico, Arizona and California where spatially extensive estimates of
 185 the ground and surface water balance components are needed to improve land and water
 186 management. The study areas include vast deserts transected by relatively narrow river corridors
 187 and a mosaic of irrigated agricultural fields and riparian vegetation (cottonwood, saltcedar,
 188 willow, mesquite, Russian olive) and native phreatophytic shrubs and grasses which creates a
 189 very heterogeneous landscape with a short patch length scale. A good SEBAL performance
 190 under these challenging conditions would be a strong indication that satisfactory performance
 191 should be expected from other types of moderate to high ET systems that are surrounded by
 192 relatively dry land uses (e.g. Compaoré et al., 2008).

193 This study involves SEBAL applications in areas without high quality hourly
 194 meteorological observations which represents a common condition for many regions worldwide
 195 (Droogers and Allen, 2002). We examined each component of the energy balance during the
 196 instant of satellite overpass and on a daily basis using a quality controlled data set consisting of
 197 ground-based R_n , H and LE measurements.

Deleted: mainly

Deleted: and

Deleted: (Tasumi, 2003;Trezza, 2002),

Deleted: is

Deleted: . Here,

Deleted: are

Deleted: valleys covered by

Deleted: salt

Deleted:)

Deleted: If

Deleted: performs well

Deleted: , it is likely to perform well in most arid and semi-arid

Formatted

Deleted: . Another difference with previous studies is our focus on all components

Deleted: as well as

Deleted: . We can accomplish this since we have available

Deleted: in the riparian areas of the Middle Rio Grande Basin (New Mexico) and R_n , G , H and LE measurements in the riparian areas of the San Pedro Basin (Arizona) and the Owens River Valley (California).

220 **2. SURFACE ENERGY BALANCE ALGORITHM FOR LAND (SEBAL)**

221 SEBAL is a remote sensing algorithm that evaluates the fluxes of the energy balance and
222 determines LE as the residual

223
$$LE = (1 - \alpha)R_s + R_{l_in} - R_{l_out} - (1 - \varepsilon_o)R_{l_in} - G - H = R_n - G - H$$

224 [1]

Deleted: $LE = R_n - G - H$

Field Code Changed

225 where R_s is the incoming shortwave radiation [Wm^{-2}], α is the surface albedo [-], R_{l_in} is the
226 incoming longwave radiation [Wm^{-2}], R_{l_out} is the emitted longwave radiation [Wm^{-2}], ε_o is the
227 surface thermal emissivity [-], R_n [Wm^{-2}], G is the soil heat flux density [Wm^{-2}], H is the sensible
228 heat flux density [Wm^{-2}], $LE (= \lambda ET)$ is the latent heat flux density [Wm^{-2}], and R_n is the net
229 radiation flux density [Wm^{-2}]. LE can be converted to the ET rate [$mmday^{-1}$] using the latent heat
230 of vaporization of water λ [Jkg^{-1}] and the density of water ρ_w [kgm^{-3}].

Deleted: R_n is the net radiation flux density [Wm^{-2}]

Formatted: Font: Italic

Deleted: and

Deleted: which

231 To implement SEBAL, images must include information on reflectance in the visible,
232 near-infrared, mid-infrared bands, and emission in the thermal infrared band. The necessary data
233 are available from a number of satellites including Land Satellite (Landsat), Moderate Resolution
234 Imaging Spectroradiometer (MODIS), Advanced Very High Resolution Radiometer (AVHRR),
235 Advanced Spaceborne Thermal Emission and Reflection Radiometer (ASTER), ENVISAT-
236 Advanced Along Track Scanning Radiometer (AATSR) and China-Brazil Earth Resources
237 Satellite (CBERS). In this study, we use Landsat images for their high spatial resolution, and
238 consistent, accurate calibration. A digital elevation model (DEM) is used to account for terrain
239 slope and aspect of each pixel. Extensive descriptions of SEBAL and METRIC have been
240 presented in the literature (Allen et al., 2011; Allen et al., 2007; Hong, 2008; Bastiaanssen et al.,
241 1998a). Critical elements of the SEBAL algorithm are discussed below.

Deleted: are needed with

Deleted: and

Deleted: as well as

Deleted: Such images

Deleted: offered by

Deleted: such as

Deleted: . In undulated landscapes

Deleted: mountains, a Digital Elevation Model

Deleted: also needed

Deleted: take into

Deleted: . Therefore, we refer to these publications and the Ph.D. dissertation by Hong (2008) for the full details of our SEBAL implementation. Here below we only discuss a critical portion of the SEBAL algorithm

260 R_n and G are determined using standard approaches similar to other energy balance
 261 remote sensing algorithms, but SEBAL and METRIC have a different unique method for the
 262 estimation of the sensible heat flux density (H). The traditional aerodynamic equation for H is
 263 between surface and air temperature measurement height (Brutsaert et al., 1993)

Deleted: LE

Deleted: defined as

Deleted: (Brutsaert et al., 1993)

$$264 \quad H = \frac{\rho_a \cdot c_p \cdot (T_{aero} - T_a)}{r_{ah}} \quad [2]$$

Deleted: $H = \frac{\rho_a \cdot c_p \cdot (T_{aero} - T_a)}{r_{ah}}$

Field Code Changed

265 where ρ_a is the density of air [kgm^{-3}], c_p is the specific heat capacity of air [$\text{Jkg}^{-1}\text{K}^{-1}$], T_{aero} is
 266 the aerodynamic surface temperature, T_a is the air temperature measured at a standard screen
 267 height, and r_{ah} is the aerodynamic resistance to heat transfer [sm^{-1}] between the surface and
 268 air temperature measurement height. SEBAL and METRIC overcome the challenge of
 269 inferring the aerodynamic surface temperature from the radiometric surface temperature and
 270 the need for near-surface air temperature measurements by directly estimating the
 271 temperature difference ΔT between T_1 and T_2 taken at two levels z_1 (0.10 m) and z_2 (2 m)
 272 above the canopy or soil surface without calculation of the absolute temperature at any given
 273 height.

Deleted:]

Deleted: a

Deleted: $H = \frac{\rho_a \cdot c_p \cdot \Delta T}{r_{ah12}}$

Field Code Changed

$$274 \quad H = \frac{\rho_a \cdot c_p \cdot \Delta T}{r_{ah12}} \quad [3]$$

Deleted: where r_{ah12} is the aerodynamic resistance between levels z_1 and z_2 . The ΔT gradient essentially 'floats' over the surface. The temperature difference for a dry surface without evaporation (the "hot" pixel) is obtained from the energy balance equation (Eq. [1]) with LE set to zero so that $H = R_n - G$ followed by the inversion of Eq. [3] to $\Delta T = H r_{ah12} / (\rho_a c_p)$. On the other hand, for a wet surface (the "cold" pixel) all available energy $R_n - G$ is assumed in traditional applications of SEBAL to be used for evapotranspiration so that $H = 0$ and $\Delta T = 0$ (Bastiaanssen et al., 1998a; Bastiaanssen, 2000). The implicit assumption in extreme-condition-inverted-calibration processes such as SEBAL and METRIC is that land surfaces with a high ΔT are associated with high radiometric temperatures and those with a low ΔT with low radiometric temperatures. Field measurements in Egypt and Niger (Bastiaanssen et al., 1998b), China (Wang et al., 1998), and USA (Franks and Beven, 1997) have shown that the relationship between T_s and ΔT is approximately positively linear for different field conditions including irrigated fields, deserts and mountains.¶

$$\Delta T = c_1 \cdot T_s + c_2$$

275 where r_{ah12} is the aerodynamic resistance between levels z_1 and z_2 . The ΔT gradient essentially
 276 'floats' over the surface. The temperature difference for a dry surface without evaporation (the
 277 hot pixel) is obtained from the energy balance equation (Eq. [1]) with LE assumed to be zero so
 278 that $H = R_n - G$ followed by the inversion of Eq. [3] to $\Delta T = H r_{ah12} / (\rho_a c_p)$. LE is set to a
 279 positive value during calibration if a daily soil water process model using precipitation inputs

306 reveals residual evaporation from prior precipitation events. For a wet surface (the cold pixel) all
 307 available energy $R_n - G$ is assumed to be used for evapotranspiration so that $H = 0$ and $\Delta T = 0$
 308 (Bastiaanssen et al., 1998a; Bastiaanssen, 2000). In METRIC, H at the cold pixel is estimated as
 309 $H = R_n - G - ET_{cold}$ where ET_{cold} is assigned a value based on scaled weather-based reference ET .
 310 The implicit assumption in extreme-condition-inverted-calibration processes such as SEBAL and
 311 METRIC is that land surfaces with a high ΔT are associated with high radiometric temperatures
 312 and those with a low ΔT are associated with low radiometric temperatures. Field measurements
 313 in Egypt and Niger (Bastiaanssen et al., 1998b), China (Wang et al., 1998), and USA (Franks and
 314 Beven, 1997) have shown that the relationship between T_s and ΔT is positive and approximately
 315 linear for a variety of field conditions including irrigated fields, deserts and mountains.

$$\Delta T = c_1 \cdot T_s + c_2 \quad [4]$$

316 where c_1 and c_2 are the linear regression coefficients valid for a landscape at the time and date
 317 the image is taken. By using the values of ΔT calculated for the cold and hot pixel, the regression
 318 coefficients c_1 and c_2 can be determined so that the extremes of H are constrained and outliers of
 319 H -fluxes are prevented. Equation [4] is dependent upon spatial differences of the radiometric
 320 surface temperature rather than absolute surface temperatures to derive maps of the sensible heat
 321 flux which minimizes the need for atmospheric corrections as well as uncertainties in surface
 322 emissivity, surface roughness and differences in T_{aero} and T_s on H estimates (Allen et al., 2007).

323 Besides ΔT the other unknown in Eq. [3] is the aerodynamic resistance to heat transfer
 324 (r_{ah12}), which is affected by wind speed, atmospheric stability, and surface roughness. Because
 325 r_{ah12} and H are interdependent, an iterative process is used to calculate H (Allen et al.,
 326 2007; Hong, 2008). After inserting R_n , G and calculated H into Eq. [1] the latent heat flux LE is

Field Code Changed

Deleted: The Eq.

Deleted: (Allen et al., 2007).

Deleted: Since

Deleted: is needed to calculate H while H is required to calculate r_{ah12}

Deleted: find H (Allen et al., 2007; Hong, 2008). Then, after

334 obtained for each pixel. Finally, dividing LE by the latent heat of vaporization of water yields the
 335 instantaneous ET (mmhour^{-1}) at the time of the Landsat overpass,

336 SEBAL and METRIC produce an estimate of the instantaneous LE at the time of the
 337 satellite overpass at approximately 10:30 am. However, for most hydrological applications the
 338 daily LE is needed, and the instantaneous LE must be extrapolated to estimate the daily LE using
 339 the instantaneous evaporative fraction (EF_{inst}). Where daily soil moisture does not significantly
 340 change and advection does not occur, the evaporative fraction has been shown to be

341 approximately constant during the day (Crago, 1996; Farah et al., 2004). However, analysis of
 342 field measurements by other investigators (Teixeira et al., 2008; Anderson et al., 1997; Sugita and

343 Brutsaert, 1991) indicates that the instantaneous evaporative fraction on clear days at satellite
 344 overpass time tends to be approximately 10 – 18 % smaller than the daytime average. Therefore,

345 a correction coefficient c_{EF} is introduced to take into account differences between instantaneous
 346 and daily evaporative fractions. Some investigators use c_{EF} of 1.00 (Bastiaanssen et al., 2005).

347 while others suggest c_{EF} of 1.10 (Anderson et al., 1997) or c_{EF} of 1.18 (Teixeira et al., 2008). The
 348 value for c_{EF} should depend on the relative amount of advection of heat, which in turn is a

349 function of regional evaporation, wind speed and relative humidity.

350
$$EF_{inst} \cdot c_{EF} = \frac{R_n - G - H}{R_n - G} \cdot c_{EF} = \frac{LE_{inst}}{LE_{inst} + H_{inst}} \cdot c_{EF} = EF_{24} = \frac{\lambda \cdot \rho_w \cdot ET_{24}}{R_{n24} - G_{24}} \cdot c_{EF} \quad [5]$$

351 Assuming daily soil heat flux G_{24} [$\text{MJm}^{-2}\text{day}^{-1}$] close to zero, multiplication of the
 352 instantaneous EF_{inst} determined from SEBAL with the total daily available energy yields the
 353 daily ET rate in mm per day (Bastiaanssen et al., 1998a)

354
$$ET_{24} = \frac{c_{EF} EF_{inst} \cdot (R_{n24} - G_{24})}{\lambda \cdot \rho_w} \approx \frac{c_{EF} EF_{24} \cdot R_{n24}}{\lambda \cdot \rho_w} \quad [6]$$

Deleted: around 10:30 am

Deleted: produces

Deleted: .

Deleted: ; so

Deleted: needs to

Deleted: which is done

Deleted: (Crago, 1996; Farah et al., 2004).

Deleted: (around 10:30 am)

Deleted: (Bastiaanssen et al., 2005) while others suggest

Deleted: (Anderson et al., 1997)

Deleted: (Teixeira et al., 2008).

Deleted: $EF_{inst} \cdot c_{EF} = \frac{R_n - G - H}{R_n - G} \cdot c_{EF} = \frac{LE_{inst}}{LE_{inst} + H_{inst}}$

Field Code Changed

Formatted: Lowered by 15 pt

Deleted: c_{EF} of 1.0 and

Formatted: Font: Italic

Deleted: (Bastiaanssen et al., 1998a) as

Deleted: $ET_{24} = \frac{EF_{inst} \cdot (R_{n24} - G_{24})}{\lambda \cdot \rho_w} \approx \frac{EF_{24} \cdot R_{n24}}{\lambda \cdot \rho_w}$

Field Code Changed

371 where ET_{24} is daily ET [~~mm day⁻¹~~], ρ_w is the density of water [~~kg gm⁻³~~] and R_{n24} is daily net
372 radiation [$MJm^{-2}day^{-1}$] obtained by an semi-empirical expression (De Bruin, 1987) as described
373 by (Hong, 2008). Finally, the daily H_{24} is not derived from the instantaneous H but is calculated
374 as the difference between R_{n24} and LE_{24} .

Deleted: mmday

Deleted: kgm

Deleted: (De Bruin, 1987)

Deleted: (Hong, 2008).

375

376 3. METHOD AND MATERIALS

377 3.1. Study Areas

378 The components of the energy balance (R_n , G , H and LE) ~~were~~ determined ~~using a~~
379 SEBAL ~~version having R_n and G components similar to those of METRIC (Allen et al., 2005).~~
380 ~~The SEBAL model was applied to~~ sixteen Landsat 7 images ~~from~~ 2000 to 2003 for three typical
381 ~~desert phreatophyte and~~ riparian areas in the southwestern United States located in the Middle
382 Rio Grande Valley (NM), the Owens Valley (CA) and the San Pedro Basin (AZ). (~~Figure 1,~~
383 ~~Table 1)~~

Deleted: are

Deleted: by

Deleted: from

Deleted: of year

Formatted: Font color: Red

384 The Middle Rio Grande Valley extends through central New Mexico and is defined as
385 the reach of the Rio Grande between Cochiti Dam and Elephant Butte Reservoir. The Middle Rio
386 Grande riparian vegetation consists of cottonwood and salt grasses as well as various non-native
387 species including saltcedar and ~~Russian~~ olive. In the Middle Rio Grande Valley, the average
388 annual air temperature is 15 °C. Daily summer temperatures range from 20 to 40 °C, ~~and~~ daily
389 winter temperatures range from -12 to 10 °C. Mean annual precipitation is about 25 cm and
390 mean annual potential evapotranspiration is approximately 170 cm.

Deleted: russian

Deleted: while

391 The Owens Valley is a long, narrow valley on the eastern slope of the Sierra Nevada in
392 Inyo County, California. It is a closed basin drained by the Owens River which terminates at

403 saline Owens Lake playa. The Owens Valley has a mild high-desert climate: in summer (June,
404 July and August) the lowest average daily minimum temperature is 7 °C and the highest average
405 daily maximum temperature temperatures is 37 °C, in winter (November to February)
406 temperature varies between -7 to 21 °C. Since, the Owens Valley is located in the rain shadow of
407 the Sierra Nevada, the average annual precipitation in the Owens Valley is only about 12 cm and
408 mean annual potential evapotranspiration is about 150 cm. Snowmelt runoff from the Sierra
409 Nevada creates a shallow water table underneath the valley floor which supports approximately
410 28,000 hectares of native phreatophytic shrubs and grasses and riparian areas.

Deleted: and

Deleted: from

Deleted: “

Deleted: ”

411 The San Pedro Basin begins in Sonora, Mexico and extends to the Gila River in southern
412 Arizona. The San Pedro River is surrounded by vegetation consisting of cottonwood, willow,
413 mesquite and sacaton grass. The mean air temperature is around 18 °C. Daily summer
414 temperatures range from 22 to 44 °C, while daily winter temperatures range from 9 to 24 °C.
415 Mean annual precipitation is about 35 cm and mean annual potential evapotranspiration is
416 approximately 170 cm.

Deleted: in

Deleted: where the river flows into

Deleted: r

Deleted: Cottonwood, Willow, Mesquite

Deleted: Sacaton

Deleted: of the Upper San Pedro valley

417 Although the regional climate of all three areas is classified as arid/semiarid, the study
418 areas have different precipitation patterns. In the Owens Valley, precipitation occurs primarily in
419 winter and spring, while in the San Pedro and the Middle Rio Grande Valleys, the annual
420 precipitation distribution is bimodal, with more than half of the rainfall being monsoonal in
421 summer, although the proportion varies considerably from year to year (Cleverly et al.,
422 2002;Elmore et al., 2002;Scott et al., 2000;Stromberg, 1998;Costigan et al., 2000). **Table 2**
423 presents main characteristics of the study sites.

Deleted: ,

Deleted: there exists a difference in

Deleted: pattern

Deleted: ,

Deleted: : vegetation type, elevation above sea level, height of vegetation canopy and the height of flux sensors above ground level. The average elevations are 1440, 1230 and 1220 m above sea level for, respectively, the Middle Rio Grande Basin, Owens Valley and San Pedro Valley.

444 **3.2. Eddy Covariance Measurements and Closure Forcing**

445 At each site, the turbulent heat fluxes were measured using the eddy covariance (EC)
446 method that theoretically provides direct and reliable measurements of H and LE (Arya, 2001).
447 At all sites, a three-dimensional sonic anemometer-thermometer that measured the three-
448 dimensional wind vector and virtual temperature, was collocated with a Krypton hygrometer or
449 open path infrared gas analyzer that measured water vapor density [gm^{-3}] with a sampling rate of
450 10 Hz (Cleverly et al., 2002; Steinwand et al., 2006; Scott et al., 2004). Covariance between the
451 vertical wind speed and water vapor density and virtual air temperature were used to compute 30
452 minutes averages of LE and H . The eddy covariance systems were oriented toward the
453 predominant wind direction to reduce interference from winds blocked by the tower and
454 instrumentation. All eddy covariance data were quality controlled and corrected for tilt by
455 coordinate rotations, frequency response, oxygen absorption of the Krypton hygrometer, and flux
456 effects on air density. The coordinate rotation, however, cannot correct for changing wind
457 direction during 30-minute average periods which can cause mean vertical wind speeds to
458 deviate from 0, thereby inducing error in the H and LE measurements. This problem is common
459 to EC measurements in tall vegetation such as trees when the sensors are placed too close to tree
460 branches or canopy. Soil heat fluxes in the San Pedro Valley and Owens Valley were obtained
461 from soil heat flux plates that were corrected for soil heat storage above the plate using
462 collocated soil temperature and soil moisture measurements.

463 At the Middle Rio Grande sites, soil heat storage could not be calculated due to the
464 absence of soil moisture measurements. Therefore, the soil heat flux measurements for those
465 sites were not compared with SEBAL estimates. Net radiation was obtained from REBS Q7 or

Deleted: SEBAL estimates of LE , H , G , and R_n are compared to ground-based eddy covariance and energy balance measurements.

Deleted: (Arya, 2001).

Deleted: measures

Deleted: ,

Deleted: measures

Deleted: The covariances

Deleted: , respectively,

Deleted: are

Deleted: for the computation of, respectively,

Deleted: the latent heat flux

Deleted: the sensible heat flux

Deleted: installed

Deleted: are

Deleted: , thereby reducing data loss due to

Deleted: effects of

Deleted: that

Deleted: 'vertical'

Deleted: where

Deleted: measurements using

Deleted: in the Middle Rio Grande Valley have

Deleted: been

Deleted: those estimated by

Deleted: . The net

490 Kipp and Zonen CNR1 net radiometers. To compare the 30-minute average ground
491 measurements with the instantaneous energy fluxes estimated using SEBAL, an instantaneous
492 ground measurement was determined by linear interpolation between the 30 minutes periods
493 before and after the satellite overpass. daily values of LE , H , G and R_n were derived by summing
494 the 30 minutes fluxes through the day (00 – 24 hours).

Deleted: In some of the installations, the R_n sensors may have been mounted too close to the towers and may have been impacted by reflection from the local structure. For the comparison of

Deleted: averaged

Deleted: 'instantaneous'

Deleted: two

Deleted: averaged, ground measurements

Deleted: To compute daily

Deleted: flux data were summed over

495 We used the relative closure of the energy balance (Twine et al., 2000) as a criterion to
496 filter the datasets to select only high-quality R_n , G , H , and LE ground measurements for
497 comparison with SEBAL estimates. Figure 2 presents the relative closures calculated for satellite
498 overpass days for all sites as provided by the investigators operating the EC towers in the Owens
499 and San Pedro River Valleys. Since no soil heat flux measurements were available in the Middle
500 Rio Grande Valley, we calculated the instantaneous relative closure [%] using the instantaneous
501 soil heat flux derived by SEBAL instead of the ground measured soil heat flux. This approach
502 was justified on the basis of the reasonable agreement found between SEBAL derived
503 instantaneous soil heat fluxes and those measured on the ground in the Owens and San Pedro
504 River Valleys (discussed below). If the sum of H and LE , before correction, was less than 65 %
505 or greater than 110 % of the available energy ($R_n - G$), the data were not used in our analysis.

Deleted: use

Deleted: (Twine et al., 2000) as a criterion for the selection of

Deleted: 1

Deleted: is

Deleted: Table 5

506 (Wilson et al., 2002) found the average energy balance closure at FLUXNET sites to be between
507 53 to 99%. Since their numbers represent average closures and since data points at the lower end
508 of the range raise greater concerns for data quality, we chose to shift the range up. Our criterion
509 excluded 45 % of instantaneous fluxes and 39 % of the daily fluxes of the data from the Middle
510 Rio Grande Valley, 79 % (instantaneous) and 43 % (daily) from the Owens Valley and 17 %
511 (instantaneous) and zero % (daily) from the San Pedro River Valley. The remaining turbulent

Deleted: This criterion leads to the exclusion of

Deleted: River

528 heat flux estimates were improved through forcing the closure of the energy balance by
529 increasing LE and H by the Bowen ratio (Twine et al., 2000). The improved adjusted H and LE
530 are identified as H_{adj} and LE_{adj} .

Deleted: are

Deleted: thru

Deleted: (Twine et al., 2000).

531 After elimination of EC measurements on the basis of unacceptable closures, we
532 eliminated also the EC measurements taken on May 16, 2003 in the San Pedro River Valley at
533 the Mesquite (CM) site, because the wind direction differed considerably from the prevailing
534 wind direction and was from a direction with very limited upwind fetch (<100 m). The problem
535 was exacerbated by the relatively high placement (7 m) of the sensors above the canopy (Table 2)
536 since the heat fluxes can vary significantly with height under such conditions (De Bruin et al.,
537 1991).

Deleted: . On this day the wind direction was approximately 90 degrees different from the prevailing wind direction which resulted in fetch distances considerably shorter than the recommended 100 times the sensor height above the canopy (Stannard, 1993; Sumner and Jacobs, 2005). The problem was exacerbated by the relatively high placement (7 m) of the sensors above the canopy (Table 2) since the heat fluxes can vary significantly with height under such conditions (De Bruin et al., 1991).

539 3.3. Scale Differences of SEBAL Flux Predictions and Ground Measurements

Deleted: Comparison

Deleted: to

Deleted: SEBAL

540 Comparison of remotely sensed (RS)-derived estimates of R_n , G , H and LE with ground
541 measurements is not straightforward because the spatial and temporal scales of the RS
542 predictions and ground measurements are quite different. In this section we will discuss the
543 effects of these scale differences on each flux in the energy balance.

Deleted: a

Deleted: operation

Deleted: SEBAL

Deleted: gaps for

544 3.3.1. Net radiation

545 R_n is measured with a net radiometer at a height of about 2 – 3 m above the canopy

546 (Table 2) that covers typically an observation area on the order of 10 m². The RS-based R_n

Deleted: measurements are taken every second and made available as 30 minutes averages for this study. The SEBAL

547 estimate is derived from reflectance in the visible, near-infrared and mid-infrared bands from a

Deleted: prediction

Deleted: reflectances

548 900 m² pixel as well as the emittance in the thermal band from a 3600 m² pixel. Details of the

Deleted: Thus, the

549 algorithms used are given in Allen et al. (2007) and are common to many applications of SEBAL

573 and METRIC. The R_n ground observation is based on a measurement area at least two orders of
 574 magnitude smaller than the RS-based prediction. For homogeneous areas the scale difference
 575 affects the comparison of ground and satellite measurements little, but for heterogeneous areas it
 576 may cause serious bias, Satellite based R_n samples a larger area and is therefore more
 577 representative of the landscape within the footprint of the eddy covariance instrument. In riparian
 578 areas, sparse vegetation with open canopies and vegetation gradients perpendicular to the river
 579 channel create a heterogeneous landscape. Radiometers are typically placed over the canopy of
 580 interest which may under-represent surrounding bare soil or ground cover within the angle of
 581 view. As a result, ground measured R_n may be biased towards the R_n of the specific vegetation,

Deleted: SEBAL

Deleted: this

Deleted: will not matter much

Deleted: , since the satellite

Deleted: EC

Deleted: .

Deleted: heterogeneity is the rule rather than exception.

582
 583 3.3.2. Soil heat flux

Deleted: cause

Deleted: representation of

Deleted: in

Deleted: Therefore

Deleted: is expected to

Deleted: of interest

584 G was measured by soil heat flux plates combined with changes in heat storage above
 585 the plate using soil temperature and soil water content measurements. If G is not corrected for
 586 heat storage above the plate, large errors will result (Sauer, 2002a). The measurement area of a
 587 soil heat flux plate is about 0.001 m² which is almost six orders of magnitude less than a 900 m²
 588 Landsat pixel. The instantaneous G can vary widely depending on soil condition (20 – 300 Wm⁻²
 589 ²), so that numerous flux measurements would be needed to estimate the average pixel G with
 590 the desired accuracy (Kustas et al., 2000;Humes et al., 1994). Therefore, we expect the
 591 instantaneous G ground measurements to be a rather crude estimation of the true instantaneous G
 592 at the scale of the pixel (Sauer et al., 2003). The impact of the scale difference on the comparison
 593 of ground and satellite measurements is somewhat mitigated by the fact that instantaneous G is
 594 positive during the day and negative during the night. Consequently, daily G is small compared

Deleted: G is measured by soil heat flux plates combined with the determination of changes in heat storage above the plate using soil temperature and soil water content measurements. If G is not corrected for heat storage above the plate, large errors will result (Sauer, 2002a). This is the case for the measurements at the Middle Rio Grande sites and, therefore, these G measurements have not been used for the comparison. The measurement area of a soil heat flux plate is about 0.001 m² which is almost six orders of magnitude less than a 900 m² Landsat pixel. G is spatially variable due to heterogeneity in soil moisture and vegetation cover, so that numerous flux measurements would be needed to estimate the average pixel G with the desired accuracy (Kustas et al., 2000;Humes et al., 1994). Therefore, we expect the instantaneous G ground measurements to be a rather crude estimation of the true instantaneous G of a pixel. The instantaneous G can vary widely depending on soil condition (20 – 300 Wm⁻²) (Sauer et al., 2003). Since G is positive during the day and negative during the night the daily G is rather small compared to the other components of the energy balance (Seguin and Itier, 1983). G is measured in the field every second; we used averages of 30 minutes for this study.¶

628 to the other components of the energy balance (Seguin and Itier, 1983).

629

630 3.3.3. Sensible and latent heat fluxes

631 At all three sites H and LE were measured using a three-dimensional sonic anemometer-
632 thermometer and a krypton hygrometer, or open patch infrared gas analyzer. For these
633 components of the energy balance the area of ground measurements is often several times larger
634 than a Landsat pixel. A typical footprint for H and LE under clear sky micrometeorological
635 conditions covers about 5 pixels or about 4500 m². The location of the footprint is upwind of the
636 EC tower, and its size depends on atmospheric stability. In the comparison of RS-based H and
637 LE estimates with ground measurements, the footprint area must be estimated and the weighted
638 average RS-estimated H and LE is computed for pixels within the footprint area. This approach
639 is expected to work reasonably well for comparison of RS-based instantaneous H and LE
640 estimates with ground measurements at the time of the satellite overpass.

641 Comparison of daily H and LE fluxes is problematic. Therefore, rather than trying to
642 determine the true location of the “representative” daily footprint, the daily H and LE ground
643 measurements are compared with the average RS-estimated H and LE fluxes originating from
644 twenty-four homogeneous pixels surrounding the EC tower. The homogeneity of the pixels
645 surrounding the tower was evaluated by inspecting NDVI, albedo, and surface temperature
646 values as well as the H and LE values themselves.

647

648 3.3.4. Quantitative measures to compare SEBAL estimates and ground measurements

649 The numerical comparison of the energy balance components (R_n , G , H , and LE)

- Deleted: are
- Deleted: Krypton
- Deleted: respectively (
- Deleted:).
- Deleted: relationship between ground measurement area and pixel size is the opposite of the one discussed for R_n and G : the
- Deleted: As discussed in Section [3.4] a
- Deleted: the
- Deleted: of this clear-sky study
- Deleted: and distance from the tower
- Deleted: For
- Deleted: SEBAL
- Deleted: first
- Deleted: determined
- Deleted: then,
- Deleted: is taken of the SEBAL
- Deleted: values of all
- Deleted: These weighted averages of H and LE are compared with the ground measured H and LE at the EC tower.
- Deleted: SEBAL
- Deleted: Instantaneous H and LE measurements are available at the EC tower as 30-minutes averages but SEBAL estimates of the instantaneous H and LE are only available once per image day at the time of the satellite overpass. Therefore, it is impossible to compare every 30 minutes the footprint averaged SEBAL estimates with the ground measurements. It is also problematic to compare daily SEBAL estimates of H and LE at each pixel with daily H and LE measurements at the EC tower. Daily H and LE measurements at the EC tower are the daily sum of 30 minutes instantaneous H and LE measurements originating from different footprints covering a wide area especially on days with highly variable wind directions. Combining the assumption of constant evaporative fraction during the day with the daily footprint using daily-averaged parameters including air temperature, u^* , wind speed and direction, it may be possible to compare daily H and LE measurements at the tower with SEBAL estimates. However, uncertainties would remain and at best a rough comparison can be made since the average daily values are not necessarily a good measure for determination of a daily footprint. Therefore, in this study
- Deleted: will be
- Deleted: SEBAL
- Deleted: five
- Deleted: ¶

693 estimated from RS with those measured on the ground was conducted by means of quantitative
 694 measures proposed by Willmott and others for the validation of atmospheric models (Willmott,
 695 1981;Fox, 1981;Willmott, 1982). We examined the coefficient of determination (r^2), mean
 696 absolute difference (MAD), root mean square difference (RMSD), and the mean relative
 697 difference (MRD) (Hong, 2008). A high or statistically significant r^2 can be misleading because
 698 its values are often unrelated to the magnitude of the differences between model estimates and
 699 measurements (Willmott and Wicks, 1980). In addition, the distributions of the estimates and
 700 measurements often do not fulfill the assumptions of inferential statistics (Willmott, 1982).
 701 However, since r^2 is a commonly used correlation measure that reflects the proportion of the
 702 variance explained by the model, we report this measure. The MAD and RMSD are robust
 703 measures as they summarize the mean differences between SEBAL estimates and ground
 704 measurements; the MAD is less sensitive to outliers than RMSD. The MRD is often used as an
 705 indication how well RS-based estimates agree with ground measurements (Bastiaanssen et al.,
 706 2005).

Deleted: by SEBAL

Deleted: is

Deleted: use

Deleted: (Hong, 2008). The coefficients of determination may be misleading as “

Deleted: ”

Deleted: of r

Deleted: sizes

Deleted: (Willmott and Wicks, 1980).

Deleted: will

Deleted: conform to

Deleted: that are prerequisite to the application

Deleted: (Willmott, 1982).

Deleted: “

Deleted: ”

Deleted: SEBAL

Deleted: (Bastiaanssen et al., 2005).

Deleted: ¶

3.4. Footprint Model¶

The location and extent of the footprint depends on surface roughness, atmospheric stability, wind speed, wind direction and may cover many pixels upwind of the eddy covariance tower (Schmid and Oke, 1990;Hsieh et al., 2000). There are several types of footprint models. Initially, simple two-dimensional analytical footprint models for neutral atmospheric conditions were developed (Gash, 1986;Schuepp et al., 1990). Later, the analytical footprint model was improved to account for atmospheric stability conditions (Horst and Weil, 1992;Hsieh et al., 2000). The footprint flux, $F_{(x, z_s)}$ [-], along the upwind direction, x [m], measured at the height z_s [m], suggested by (Hsieh et al., 2000) is used in this study. ¶

3.4. Footprint Model

The location and extent of the footprint depends on surface roughness, atmospheric stability, wind speed, wind direction and may cover many pixels upwind of the eddy covariance tower (Schmid and Oke, 1990;Hsieh et al., 2000). The footprint flux, $F_{(x, z_s)}$ [-], along the upwind direction, x [m], measured at the height z_s [m], suggested by (Hsieh et al., 2000) was used in this study.

A typical footprint size and footprint intensity for one 30 minute period on August 19,

745 2002, at a Rio Grande saltcedar EC tower is presented in [Figure 3](#). To verify the quality of the
 746 footprint model used in this study, we also calculated [the location of maximum contribution to](#)
 747 [the measured flux \(\$x_{max}\$ \)](#) for this period with the model by Schuepp et al. (1990) . The models by
 748 Hsieh et al (2000) and Schuepp et al. (2000) calculate x_{max} as 10 m ([Figure 3](#)) and 11 m,
 749 respectively, which implies that the footprint from Hsieh et al (2000) is indeed close to the tower.
 750 At most EC sites, the maximum contribution to the footprint was within 50 m from the tower
 751 (wind speeds were generally less than 4 ms^{-1}) and most of the footprint intensity (>90 %) is
 752 located within 300 m from the tower. [Approximately 80 % of all footprint fluxes cover an area of](#)
 753 [5 to 9 pixels, twenty percent cover larger areas. Because calculation of a representative daily](#)
 754 [footprint for \$H\$ and \$LE\$ is nearly impossible, the average RS daily \$H\$ and \$LE\$ values of the 24](#)
 755 [pixels surrounding the EC tower pixel are used for comparison with daily ground measurements.](#)

Deleted: 2

Deleted: (peak footprint)

Deleted: 2

Deleted: We compute the footprints from meteorological parameters including air temperature, sensible heat flux, wind speed, wind direction and friction velocity. The footprints for H and LE are obtained for the time of the satellite overpass using the 30 minute averaged meteorological parameters.

Deleted: As explained in [Section \[3.3.3\]](#)

Deleted: comparison of SEBAL

Deleted: estimates and ground measurements

Deleted: . Therefore, the use

Deleted: 25

Deleted: is considered to be the best option

Deleted: the

Deleted: of

Deleted: and SEBAL estimates.

Deleted: ¶

Deleted: SEBAL

Deleted: This study cannot be a robust validation study due to missing soil heat flux measurements in the Middle Rio Grande Valley and biased net radiation measurements over heterogeneous riparian vegetation with patches of bare soil. Our aim is to evaluate the challenges of SEBAL flux predictions in arid riparian areas using a validation approach.¶

Calibration is the process of adjusting hydrologic model parameters to obtain a fit to observed data. In SEBAL the relationship between model parameter ΔT and remotely observed radiometric surface temperature T_s in [Eq. \[4\]](#) is calibrated using the remotely observed energy balance components of R_n and G at two extreme conditions in a Landsat image: the cold wet pixel and hot dry pixel. ¶ After calibration, validation tests typically are applied to a second set of data to test the performance of a hydrologic model. In the context of this study the second data set consists of ground measurements of R_n , G , H and LE , at pixels other than the cold and hot pixels. Validation or evaluation is accomplished by comparing the SEBAL predicted energy balance components with the ones measured on the ground at locations with eddy covariance towers. ¶

¶ 3.5.1 Calibration approaches¶

The temperatures of the cold and hot pixel for the derivation of calibration coefficients c_1 and c_2 in [Eq. \[4\]](#) are most critical in SEBAL as well as METRIC since they constrain LE between its maximum value at the cold wet pixel and zero at the hot dry pixel by reducing biases in H associated with uncertainties in aerodynamic characteristics including T_s (Bastiaanssen et al., 2005; Allen et al., 2006). In SEBAL this calibration is entirely based on information that is available inside the image and, therefore, it is called “self-calibration” (Bastiaanssen et al., 2005) or “internalized calibration” and “autocalibration”. ¶ Over

757 3.5. Calibration and Evaluation of [RS-based Flux Predictions](#)

758 [The temperatures of the cold and hot pixel for the derivation of calibration coefficients \$c_1\$](#)
 759 [and \$c_2\$ in \[Eq. \\[4\\]\]\(#\) are critical in SEBAL and METRIC because they constrain \$LE\$ between its](#)
 760 [maximum value at the cold wet pixel and near zero at the hot dry pixel. The coefficients also](#)
 761 [incorporate and compensate for bias in \$H\$ associated with uncertainties in aerodynamic](#)
 762 [characteristics including \$T_s\$ \(Bastiaanssen et al., 2005; Allen et al., 2006\). In SEBAL and](#)
 763 [METRIC this calibration is entirely based on information available within the image and is](#)
 764 [variously referred to as self-calibration \(Bastiaanssen et al., 2005\) or internalized calibration and](#)
 765 [autocalibration.](#)

766 [At the cold pixel it is assumed in SEBAL that \$\Delta T = 0\$, which implies that \$H = 0\$ and \$LE =\$](#)

818 $R_n - G$. An alternative manner in METRIC is to use hourly meteorological observations for the
 819 calculation of the reference ET (Allen et al., 1998) for the estimation of H in well-irrigated
 820 alfalfa or clipped grass fields (Allen et al., 2007; Allen et al., 2011). However, this study deals
 821 with a SEBAL application to riparian areas without high quality hourly meteorological
 822 observations as is the default condition for many regions worldwide (Droogers and Allen, 2002).
 823 The selection of the hot pixel is challenging because the heterogeneous landscapes of the
 824 southwestern U.S. include hot and dry areas with a wide range of temperatures. In this study, the
 825 hot pixel was selected from a dry bare agricultural field where ET can reasonably be assumed to
 826 be near zero. Any pixel cooler than the selected hot pixel has $ET > 0$ (if the R_n and G are the
 827 same), and for any pixel warmer than the hot pixel, for example parking lots, $ET = 0$. In addition,
 828 the equation to estimate G_v was derived for agricultural conditions and therefore produces more
 829 dependable estimates for calibration when applied to a bare, agricultural soil having a tillage
 830 history.

Deleted: high quality

Deleted: (Allen et al., 1998)

Deleted: and

Deleted: (Allen et al., 2007; Allen et al., 2011).

Deleted: in

Deleted: (Droogers and Allen, 2002).

Deleted: quite

Deleted: quite a few

Deleted: is

Deleted: is just close to

Deleted: Therefore, for any

Deleted: ,

Deleted: a

Deleted: for

Deleted: estimation

831 As a consequence of the internalized calibration, bias in R_n or G at the hot pixel in the
 832 image are transferred into H . However, the bias is present in both $R_n - G$ and H (Eq. [1]), and
 833 thus cancels out in the calculation of LE (Allen et al., 2006). The internalized calibration results
 834 in the least biased LE if the cold and hot pixel are properly selected and is the most distinctive
 835 feature of SEBAL and METRIC compared to other remote sensing LE algorithms.

Deleted: "

Deleted: " any biases

Deleted: this bias introduced into H is transferred back out of the energy balance during the calculation of LE from Eq. [1], since

Deleted: ,

Formatted: Font color: Red

Deleted: (Allen et al., 2006). The "internalized calibration"

836 The selection of cold and hot pixel is assisted by a thorough understanding of field
 837 micrometeorology and is somewhat subjective (Kleissl et al., 2009) proposed using
 838 micrometeorological ground measurements of energy balance components for the calibration and
 839 validation of remote sensing algorithms. However, due to the relatively large uncertainties of

Deleted: requires

Deleted: , i.e. different experts will select slightly different temperature values. The cold pixel is selected where areas with well-watered healthy crops with full soil cover or in shallow water bodies (Allen et al., 2011; Bastiaanssen et al., 2005) and is relatively straightforward while the hot pixel selection is more challenging. Therefore, it has been

Deleted: to use

Deleted: such as SEBAL (Kleissl et al., 2009).

870 ground measured sensible and latent heat fluxes (Loescher et al., 2005; Kleissl et al., 2008) the

Deleted: (Loescher et al., 2005; Kleissl et al., 2008)

871 value of using ground measurements for calibration of SEBAL is not well established. We tested

Deleted: For this reason we test

872 two different calibration approaches for the selection of the temperatures for the cold and hot

873 pixel: the Empirical (EM) approach and the Eddy Covariance (EC) approach. The former selects

Formatted: Font: Not Italic

Deleted: is based on

Formatted: Font: Not Italic

874 the cold and hot pixel by inspection of the hydrogeological features of the landscape and

875 qualitative micrometeorological considerations and is typical for most SEBAL applications. The

Deleted: since the high number of EC towers available in this study is a unique situation.

876 Eddy Covariance (EC) approach is based on inspection of the hydrogeological features of the

Formatted: Font: Not Italic

Formatted: Font: Not Italic

877 landscape followed by fine-tuning the parameters c_1 (slope) and c_2 (intercept) in Eq. [4] using

878 ground measurements of instantaneous latent heat fluxes at the EC towers after adjustment for

879 energy balance closure. This approach is viable because of the large number of ground based

Deleted: error. Since selection

Deleted: cold pixel is straightforward

880 measurements in this study. The temperature of the cold pixel was fixed by selecting a pixel in

Deleted: fully vegetated fields, the

Deleted: but the

881 fully vegetated fields, but the selection and temperature of the hot pixel was varied to best match

882 the instantaneous ground measurements of LE (Hong, 2008).

Deleted: (Hong, 2008). In order to independently evaluate the EM versus the EC approach, senior author Hong implemented the EC approach, while co-author Hendrickx implemented the EM approach.

883 Five different calibration scenarios (S1 – S5) were compared (Table 3). In the EC

Formatted: Indent: First line: 0.5", No widow/orphan control, Don't adjust space between Latin and Asian text, Don't adjust space between Asian text and numbers

884 approach, calibration of SEBAL to ground measurements was implemented either using the

Deleted: implemented and

885 average footprint weighted instantaneous SEBAL LE heat fluxes (S1, EC_FP) or using the

Formatted: Font: Not Italic

886 instantaneous SEBAL LE heat flux of the pixel where the EC tower was located (S2, EC_TP).

Deleted: is

887 The former method is difficult to implement for most practitioners while the latter is practical

888 and fast but requires homogeneous conditions around the tower within the maximum extent of

Deleted: to

889 the footprint. The EM approach (S3) was implemented without using the LE 's measured by the

Formatted: Font: Not Italic

890 EC towers or any other meteorological measurements. In Section [3.3.1] we hypothesized that

Deleted: ¶

Deleted: it was

891 the ground measured R_n may be biased towards vegetation while the SEBAL R_n may be more

910 representative for the true R_n of a pixel covered with vegetation and bare soil patches. Initial
 911 results suggested that the (SR_n) is more representative than ground R_n . Therefore, we also
 912 evaluated the impact of using the more accurate SR_n for energy balance closure in the EC
 913 approach on the tower pixel (S4, EC_TP/SR_n) and in the EM approach (S5, SR_n).

Deleted: In Section [4] strong evidence is presented

Deleted: SEBAL R_n

Deleted: accurate

Formatted: Font: Not Italic

Formatted: Font: Not Italic

915 4. RESULTS AND DISCUSSION

916 4.1. Spatio-temporal Distribution of Daily Latent Heat Fluxes

917 Figure 4 presents an example of daily ET rates in the Middle Rio Grande Valley and
 918 surrounding desert on four different days during the spring, summer and fall. The maps show
 919 how the ET rates increase from April 7 (just after the start of the irrigation season) to June 16 at
 920 the height of the irrigation season; a decrease of ET is observed during September and October
 921 when fields were harvested and lower temperatures impede crop growth. On all four days higher
 922 ET rates were observed over irrigated fields and in the riparian areas while low to zero rates
 923 occurred in the surrounding desert.

Deleted: 3

Deleted: the ET maps produced by SEBAL. Similar maps for the other components of the energy balance as well as other environmental parameters such as albedo, NDVI, surface temperature, etc. can be generated. In Figure 3,

Deleted: are mapped

Deleted: deserts

Deleted: are

Deleted: are impeding

Deleted: are

Deleted: very low

Deleted: occur

Deleted: deserts

Deleted: SEBAL

Deleted: 4

Deleted: 5

925 4.2. Comparison of RS-Based Net Radiation with Ground Measurements

926 Figures 5 and 6 and Table 4 present the comparisons of the instantaneous and daily R_n
 927 measured on the ground and estimated by SEBAL. MADs for the EC approaches (S1/S2) and
 928 Empirical Approach (S3) were 88/87 and 97 W/m², respectively; MRDs were 13.0/12.8 and
 929 14.6%. These differences are about two to three times larger than those typically reported for
 930 SEBAL (Jacob et al., 2002; Allen et al., 2006). The much larger MRD was attributed to the
 931 heterogeneity of the riparian sites and the different footprints of net radiometer and Landsat pixel

Deleted: The MADs are 88/87 and 97 W/m² for the EC approaches (S1/S2) and Empirical Approach (S3), respectively, resulting in MRDs of 13.0/12.8 and 14.6%. These differences are about two to three times larger than those typically reported for SEBAL (Jacob et al., 2002; Allen et al., 2006). The much larger than usual MRD is attributed to the heterogeneity of the riparian sites, the different footprints of net radiometer and Landsat pixel, and the preferential positioning of the net radiometer over vegetation (Section [3.3.1]). The higher net radiation measured on the ground as compared with the SEBAL net radiation supports this argument. A bias occurs where the net radiometer is placed preferentially above vegetation that has a lower albedo, lower surface temperature and higher surface emissivity than the patches of bare soil next to the vegetation in the Landsat pixel. Increasing MRDs with increasing heterogeneity of the land surface have been observed in Arizona where the MRD's between ground measured R_n 's and the one's estimated with a remote sensing algorithm were 1.2, 9.2, and 17.2 %, respectively, for a homogeneous cotton field, heterogeneous shrub terrain, and heterogeneous grassland (Su, 2002). The MRD of 9.2 and 17.2 % from the heterogeneous pixels are similar to the ones reported in Table 4.

972 (Section [3.3.1]). Higher net radiation measured on the ground compared with the RS-based R_n
973 supports this argument. The MRDs of 9.2 and 17.2 % from (Su, 2002) on heterogeneous pixels
974 of shrub and grassland vegetation are similar to the ones reported in this study (Table 4).

975 Contrary to the instantaneous values, the daily net radiation measured on the ground and
976 determined in SEBAL match very well (MRDs of -2.3 to -2.9%). This immediately begs the
977 question “why?” since the instantaneous R_n differ by more than 12%. On clear days over sparsely
978 vegetated surfaces the maximum temperature difference between bare soil and vegetation
979 typically occurs around noon. For example, temperature differences measured in the Walnut
980 Gulch Experimental Watershed near Tombstone, Arizona, varied between 10 and 25 °C during
981 that time of the day (Humes et al., 1994). Since the conditions in the arid riparian areas of this
982 study are similar, we expect similar temperature differences to occur when the satellite passes
983 over around 10:30 am. The incoming short and longwave radiation are equal for the bare soil and
984 the vegetation; therefore, the net radiation will depend on the outgoing short and long wave
985 radiation. The albedo and surface temperature of dry bare soils during the day are higher than of
986 vegetation resulting in more reflection of short wave radiation and more emission of long wave
987 radiation which results in a lower R_n through the day for bare soil. During the night the surface
988 temperatures of vegetation and bare soil are similar. However, due to the higher emissivity of
989 vegetation (0.99) as compared to bare soil (0.94) (Humes et al., 1994), the R_n of vegetation is
990 lower. (Hong, 2008) calculated that the daily R_n difference between vegetation and soil will be
991 considerably smaller than the instantaneous R_n difference around 10:30 am.

992 Differences between vegetation and soil have been quantified by comparing the RS-
993 estimated instantaneous and daily net radiation for fully vegetated agricultural fields, saltcedar,

Deleted: radiations

Deleted: with

Deleted: only

Deleted: %.

Deleted: R_n 's

Deleted: (Humes et al., 1994).

Deleted: during

Deleted: so that –

Deleted: (Humes et al., 1994) – the R_n of vegetation is lower. Using the equations presented by (Hong, 2008) one can roughly calculate

Deleted: These differences

Deleted: SEBAL

1007 and bare soils (Table 5). Whereas the measured instantaneous net radiation fluxes of fully
 1008 cropped agricultural fields and saltcedar stands exceeded those of bare soils by 54 to 77 %, the
 1009 daily net radiation fluxes were only 20 to 36 % larger. A typical leaf area index (LAI) for
 1010 saltcedar in the Middle Rio Grande Valley is about 2.5 (Cleverly et al., 2002) which indicates
 1011 that bare soil is present but vegetation cover is dominant. Assume a typical mixed pixel with a
 1012 soil cover of 75% saltcedar and 25% bare soil. The data from Table 5 for the first saltcedar plot
 1013 show that the ratios between 100% saltcedar and 100% bare soil for instantaneous and daily R_n
 1014 are 1.77 and 1.34. We want to estimate ratios between 100% saltcedar and a hypothetical mixed
 1015 pixel. Using the values in Table 5 for the instantaneous and daily R_n for saltcedar and bare soil,
 1016 and ignoring the effect of thermal radiation from soil that is intercepted by adjacent vegetation,
 1017 the instantaneous and daily R_n for the mixed pixel are $0.75 \times 670 + 0.25 \times 379 = 598 \text{ Wm}^{-2}$ and
 1018 $0.75 \times 19.8 + 0.25 \times 14.8 = 14.9 + 3.7 = 18.6 \text{ MJm}^{-2}\text{day}^{-1}$. The net instantaneous and daily R_n of
 1019 a fully vegetated saltcedar pixel are $670/598 = 1.12$ and $19.8/18.6 = 1.06$ times those of the
 1020 hypothetical mixed pixel. The 12% difference is similar to the MRD's of 13 – 15% for the
 1021 difference in instantaneous R_n between ground measurements and RS-based estimates (Table 4).
 1022 The 6% difference for daily R_n falls within error ranges of radiation measurements (Halldin and
 1023 Lundroth, 1992; Field et al., 1992). Thus, the much smaller MRD for daily R_n (-2.3 to -2.9 %)
 1024 compared to the MRD of instantaneous R_n (about 13 %) can be explained by environmental
 1025 radiation physics and is not an artefact of bias in the RS method or in the ground-based radiation
 1026 sensors. This corroborates our interpretation that the RS-estimated net radiation for the 900 m² of
 1027 the EC tower pixel is more representative for each site than the ground measurements with the
 1028 net radiation meter preferentially positioned over a 10 m² patch of vegetation.

Deleted: Leaf Area Index

Deleted: (Cleverly et al., 2002) which indicates that bare soil is present but vegetation cover is dominant. Now let us assume

Deleted: , respectively,

Deleted: net radiation

Deleted: find similar

Deleted: our

Deleted: using

Deleted: of

Deleted: net radiation

Deleted: . Ignoring

Deleted: net radiations

Deleted: , respectively,

Deleted: So, the

Deleted: radiations

Deleted: our

Deleted: percent

Deleted: presented

Deleted: net radiation

Deleted: SEBAL

Deleted: .

Deleted: percent

Deleted: net radiation

Deleted: (Halldin and Lundroth, 1992; Field et al., 1992). Thus, the much smaller MRD for daily R_n (-2.3 to

Deleted: caused by

Deleted: SEBAL

Deleted: for determination of instantaneous R_n

Deleted: leads to the conclusion

Deleted: SEBAL

Deleted: ¶

1060
1061
1062
1063
1064
1065
1066
1067
1068
1069
1070
1071
1072
1073
1074
1075
1076
1077
1078
1079
1080
1081

4.3. Comparison of RS-estimated Soil Heat Flux with Ground Measurements

The magnitude of soil heat flux, G_s , depends on surface cover, soil water content, and solar irradiance. For a moist soil beneath a plant canopy or residue layer, the instantaneous G will often be less than $\pm 20 \text{ Wm}^{-2}$ (Sauer, 2002b) while a bare, dry, exposed soil in midsummer could have a day-peak in excess of 300 Wm^{-2} (Fuchs and Hadas, 1973). In the Middle Rio Grande Basin during summer typical midday (10 am through 2 pm) values of G averaged 104 and 132 Wm^{-2} for upland grassland and shrubs, respectively (Kurc and Small, 2004). Instantaneous G in riparian areas is an important component of the energy balance that needs to be taken into account.

For this study six soil heat flux measurements were available from the Owens Valley and the San Pedro Valley data set. The RS-determined G approximates the ground measured G reasonably well (Figure 7) but the MRD is relatively high with values of 30.9 to 32.2 % (Table 6). However, the overall impact of the relatively high MRD in instantaneous G is relatively small since the MAD (35 Wm^{-2} , Table 6) is only 6 % of the RS-predicted instantaneous net radiation and 5% of the ground measured instantaneous R_n . The daily G is near zero since heat enters the soil during the day but leaves the soil during the night (Table 6).

Given the high spatial and temporal variability of G (Sauer, 2002b) at the scale of a Landsat pixel, the reasonable agreement between RS-predicted instantaneous G and ground measurements, the relatively minor impact of an error in G on the estimates of ET , and the impracticality of measuring a truly representative G for a 900 m^2 heterogeneous pixel, it appears that assuming G is negligible within SEBAL and METRIC is acceptable.

- Deleted: SEBAL
- Deleted: (Sauer, 2002b)
- Deleted: (Fuchs and Hadas, 1973).
- Deleted: are
- Deleted: , respectively,
- Deleted: (Kurc and Small, 2004). These values demonstrate that the instantaneous
- Deleted: can be
- Deleted: instantaneous
- Deleted: In most field soils the instantaneous G exhibits not only a temporal variability but also a large spatial variability which makes it very difficult to measure an average G for areas with the size of a typical Landsat pixel (30 x 30 m) (Sauer, 2002b).
- Deleted: SEBAL
- Deleted: approaches
- Deleted: 6
- Deleted: minor
- Deleted: its
- Deleted: of
- Deleted: (
- Deleted: hovers around
- Deleted: percent
- Deleted: SEBAL
- Deleted: around
- Deleted: percent
- Formatted: Font: Italic
- Deleted: net radiation.
- Deleted: close to
- Deleted: . The daily G measurements in the field confirm this
- Formatted: Font color: Auto
- Deleted: Therefore, it is assumed in SEBAL that the daily heat flux can be neglected, i.e. G is zero.
- Deleted: (Sauer, 2002b) within one
- Deleted: SEBAL
- Deleted: (Figure 6 and Table 6),
- Formatted: Font: Italic
- Deleted: impossibility to measure
- Deleted: riparian
- Deleted: using soil heat flux plates with a foot print of only 0. (...)
- Deleted: the SEBAL estimated
- Deleted: results in a quite
- Deleted: estimate on the pixel scale.

4.4. Comparison of RS-based Sensible and Latent Heat Fluxes with Ground Measurements

Our data set covers a wide range of conditions varying from dry to moist which allows evaluation of SEBAL over a wide range of environmental conditions in riparian areas. Plots of instantaneous and daily SEBAL heat flux estimates versus ground measurements are presented in Figure 8. The ground measured instantaneous and daily H have two and six negative data points indicating regional advection. Advection is relatively minor for the instantaneous fluxes during satellite overpass time of around 10:30 am but increases considerably during late morning and early afternoon. The SEBAL estimated instantaneous and daily H that correspond with negative values of the ground measurements are near zero since the surface temperatures of the pixels are similar to the cold pixel temperature. When high quality hourly meteorological data are available regional advection can be accounted for in SEBAL by defining an advection enhancement parameter that is a function of soil moisture and weather conditions (Bastiaanssen et al., 2006; Allen et al., 2011) or one could implement METRIC (Allen et al., 2007), which has an implicit handling of advection due to its use of Penman-Monteith-based reference ET. However, in this study our aim is to evaluate the performance of the original SEBAL in heterogeneous arid environments where no weather data are used. The data in Figure 8 show that ignoring regional advection results in a maximum underestimation of the instantaneous and daily LE by, respectively, about 10 and 20% under moist conditions and when $C_{EF} = 1.0$; it becomes considerably less when the soil dries out. In this study we have removed all data related to negative instantaneous and daily H so that advection effects will not interfere with our evaluation of the original SEBAL approach (Allen et al., 2011; Bastiaanssen et al., 1998a).

Deleted: SEBAL

Deleted: Since there is a strong interplay between sensible and latent heat fluxes we discuss both heat fluxes together in this section. First we inspect the plots of instantaneous and daily SEBAL heat flux estimates versus ground measurements (Figure 7) that demonstrate several interesting features.

Deleted: 7

Deleted: sensible heat fluxes

Deleted: , respectively,

Deleted: which is an indication of the occurrence of

Deleted: This advection

Deleted: m

Deleted: as reflected in the daily fluxes.

Deleted: sensible heat fluxes

Deleted: to

Deleted: close to

Deleted: their

Deleted: close

Deleted: pixel's

Deleted: (Bastiaanssen et al., 2006; Allen et al., 2011)

Deleted: (Allen et al., 2007).

Deleted: traditional

Deleted: available

Deleted: 7

Deleted: latent heat fluxes

Deleted: percent

Deleted: sensible heat fluxes

Deleted: traditional

Deleted: that does not take advection into account (Allen et al., 2011; Bastiaanssen et al., 1998a).

1175 4.4.1. Comparison of instantaneous heat fluxes

1176 Figures 9 and 10 present plots of the adjusted H and LE measured at the EC tower versus
1177 the SEBAL estimates for scenarios S1 through S5. There was a substantial mismatch between
1178 the SEBAL estimated instantaneous H and the ground measurements (S1–S3), but if the SEBAL
1179 R_n is used in the ground measured energy balance, the correspondence was much improved (e.g.
1180 scenarios S4 and S5 in Figure 9). This is due to the bias-correction strategy of SEBAL and
1181 METRIC where biases in R_n and G are incorporated into estimates for H . SEBAL estimated
1182 instantaneous LE and ground measurements show good agreement for all five scenarios (S1 – S5)
1183 including the ones with a poor sensible heat flux match (Figure 10, S1-S3). The prediction of LE
1184 is good for scenarios S1–S5 with a mean MRD of -5.1% (Table 7) which is less than the average
1185 14% deviation reported for SEBAL applications worldwide (Bastiaanssen et al., 2005).

1186 The ground measured instantaneous H and LE presented in Table 7 are identical in S1–
1187 S3 but differ slightly from each other in S4 and S5 due to a slight difference in the temperature
1188 of the cold pixels that were chosen to estimate air temperature for calculation of the incoming
1189 long wave radiation. As a result the instantaneous net radiation used in scenarios S4 and S5 were
1190 also slightly different. However, a large difference existed between the ground measured H and
1191 LE in S1–S3 versus those in S4–S5 caused by the bias in instantaneous R_n of the ground
1192 measurements versus R_n determined with SEBAL (Table 4). In Table 7 the H and LE from
1193 SEBAL for the EM approaches (S3 and S5) are identical because EC measured instantaneous LE
1194 was not used for calibration; one set of cold and hot pixels are used for both scenarios. However,
1195 for S1, S2 and S4 a different set of cold and hot pixels were chosen for each scenario by forcing

- Deleted: 8
- Deleted: 9
- Deleted: , respectively,
- Deleted: sensible
- Deleted: latent heat fluxes
- Deleted: towers
- Deleted: resulting from
- Deleted: While there exists
- Deleted: severe
- Deleted: sensible heat fluxes
- Deleted: once
- Deleted: estimated net radiation
- Deleted: “
- Deleted: ”
- Deleted: good agreement is reached (
- Deleted:).
- Deleted: 8
- Deleted: latent heat fluxes
- Deleted: 9
- Deleted: Table 7 presents the quantitative comparison measures for these instantaneous fluxes.
- Deleted: latent heat fluxes
- Deleted: instantaneous
- Deleted: (Bastiaanssen et al., 2005).
- Deleted: pixel that is also used for the estimation of the
- Deleted: radiations of
- Deleted: are
- Deleted: exists
- Deleted: . This is
- Deleted: net radiation
- Deleted: the net radiation
- Deleted: estimates
- Formatted: Font: Not Italic
- Deleted: since this approach does not use the
- Deleted: in SEBAL
- Deleted: in
- Deleted: are determined

1232 the constants c_1 and c_2 in Eq. [4] to fit the instantaneous LE measurements at the EC towers. This

1233 produced quite different H and LE SEBAL estimates for S1, S2 and S4.

1234 In scenarios S1 and S2 of Table 7 there is no significant difference between the SEBAL

1235 estimated H (156 versus 138 W/m^2) and LE (314 versus 333 W/m^2). SEBAL calibrations based

1236 on the instantaneous LE of the tower pixels (S2) or on the LE of the instantaneous foot prints

1237 during the satellite's overpass (S1) yielded similar results except that the MAD and RMSD of S1

1238 were lower. (MAD/RMSD values for S1 and S2 were 39/57 and 56/74, respectively). This

1239 finding is relevant for practitioners who need to calibrate SEBAL on a routine basis and/or in

1240 nearly real-time. Using only the tower pixel is much faster and easier to implement automatically

1241 than determination of a weighted average within the tower footprint. However, for *posterior*

1242 SEBAL analyses and research applications use of the footprint is still recommended because (1)

1243 it has a better correspondence with ground measurements (Table 7) and (2) footprint analyses are

1244 effective for the detection of unusual environmental conditions.

1245 The MAD and RMSD of H for S1, S2 and S3 are quite similar but rather high with

1246 MAD/RMSD values of 108/131, 126/147 and 111/135, respectively. The values of S4 and S5

1247 (36/46 and 61/77) are considerably lower reflecting the ground energy balance correction by

1248 relying on the RS-based R_n . The MAD/RMSD values of the LE range from values of 39/57 for

1249 S1, 56/74 for S2, and 66/81 for S3. Values for S4 and S5 (39/48 and 61/77) were similar to S1,

1250 S2, and S3. Using the RS-based R_n had a much smaller effect on LE estimates than the H

1251 estimates which is a consequence of the internal calibration of SEBAL, and METRIC.

1252 MRD values exhibited the same trends observed in the MAD and RMSD values (Table

1253 7). A striking feature in S1–S3 is the very poor prediction of H : with MRD's were between 35

Deleted: leads to

Deleted: in

Deleted: sensible

Deleted: latent

Deleted:) heat fluxes. Thus,

Deleted: latent heat flux

Deleted: latent heat flux

Deleted: yield

Deleted: in this study

Deleted: are

Deleted: :

Deleted: are

Deleted: .

Deleted: : using

Deleted: pixels

Deleted: footprint

Deleted: . It also justifies

Deleted: omission of foot print scenario S1 from further consideration in scenario S4

Deleted: since (1) it results in somewhat smaller comparison measures

Deleted: the sensible heat fluxes

Deleted: , respectively,

Deleted: .

Deleted: and reflect

Deleted: using

Deleted: SEBAL net radiation

Deleted: latent heat fluxes are increasing

Deleted: a low value

Deleted: to

Deleted: while the values

Deleted: are, respectively,

Deleted: . Thus, using the net radiation correction has

Deleted: for the latent heat fluxes

Deleted: for

Deleted: sensible heat fluxes

Deleted: result

Deleted: . The comparison measures for S3

1292 and 47 %. This result was not expected, especially, for S1 and S2 that were calibrated against
1293 ground measured instantaneous LE. The discrepancy was the result of the apparent bias in the
1294 ground measurements of R_n , discussed previously (see Section [4.2]). Substituting the RS-based
1295 R_n for the ground measured R_n improved the RS-based estimates of H dramatically: MRD's of
1296 S4 and S5 were 0.8 and 16.6 %, respectively. Despite the poor MRD's of H (35 to 47 %), in S1 –
1297 S3, the SEBAL LE estimates exhibited good MRD's (2.7 to -11.5 %). Although RS-based
1298 estimates of H had high error, the internal calibration procedure protects against inaccurate
1299 estimates of LE .

Deleted: (the empirical traditional

1300 Calibrating SEBAL with reliable ground measurements at the pixel scale improved
1301 estimates of both H and LE . However, ground measurements of H should be used cautiously and
1302 carefully for the calibration and evaluation of SEBAL because the RS-based H estimate
1303 compensates for error in R_n , G , and aerodynamics, and can deviate from the ground-based
1304 measurements. Lumping error into H is a necessary characteristic of SEBAL and METRIC
1305 designed to arrive at unbiased estimates for LE .

Formatted: Tab stops: 2.22", Left

Deleted: approach) are also very similar for the latent heat flux but are reduced in half for the sensible heat flux after net radiation correction.

1306 The internal calibration of H and LE using cold and hot pixels in SEBAL and METRIC
1307 reduces or cancels bias introduced by the calculation of albedo, net radiation, and surface
1308 temperature as well as errors in narrow band emissivity, atmospheric correction, satellite sensor,
1309 aerodynamic resistance, and soil heat flux. This procedure can result in a reduction of total bias
1310 in ET of as much as 30 % compared to other models that are not routinely internally calibrated
1311 (Allen et al., 2006). Allen et al. (2007) describe how METRIC, through the use of weather based
1312 reference ET, is able to eliminate most internal energy balance component biases at both the cold
1313 and hot extreme conditions. SEBAL, on the other hand, eliminates bias at the hot extreme, but

Deleted: Through the "anchoring"

Deleted: at the

Deleted: biases

Deleted: in

Deleted: function

Deleted: (Allen et al., 2006).

Deleted: biases

1325 necessarily retains a bias at the cold extreme where it is assumed that $LE = R_n - G$. The cost for
 1326 the improved estimates for LE is a deterioration of the SEBAL and METRIC H estimates since H ,
 1327 as an intermediate parameter, absorbs most of the aforementioned bias as a result of the internal
 1328 calibration process (Choi et al., 2009).

1330 4.4.2. Comparison of daily sensible and latent heat fluxes

1331 The ground measured daily evaporative fraction (EF_{24}) is larger than the instantaneous
 1332 evaporative fraction (EF_{inst}) (Figure 11). A simple linear regression yielded a small not
 1333 significant intercept of 0.04 ($p > 0.05$) and a slope of 1.19 (95 % confidence interval 0.99 to 1.36).
 1334 The traditional SEBAL application assumes $c_{EF} = 1.0$ (Bastiaanssen et al., 1998a), but several
 1335 field studies suggest the value is closer to 1.1 (Brutsaert and Sugita, 1992; Anderson et al., 1997).
 1336 While recognizing that 1.19 is closer to 1.1 than to 1.0, we examined the effects of both
 1337 estimates for c_{EF} on the conversion from instantaneous LE to daily LE (see Eq. [5]).

1338 Figures 12 and 13 present the plots of the adjusted (using ground measured R_n energy
 1339 balance closure) H and LE daily heat fluxes measured at the EC towers versus the SEBAL
 1340 estimates resulting from scenarios S1–S3 with c_{EF} set to 1.1. Scenarios S4 and S5 are not shown
 1341 because the daily R_n measured on the ground and determined by SEBAL were similar (Table 4).
 1342 For the values in Table 8, when the $c_{EF} = 1.0$, the agreement was excellent for the daily LE
 1343 (mean MRD of 3.9% = $[2.9 + 0.0 + 8.9]/3$) but was rather poor for the H (mean MRD of -20.4% =
 1344 $[-19.4 - 14.9 - 27.0]/3$). Next, using a c_{EF} value of 1.1, SEBAL estimated LE increased, therefore
 1345 MRDs (MRD = $(\bar{G} - \bar{S})/\bar{G}$) of LE decreased to be negative so that MRDs of H improved (less
 1346 negative). As a result, the assumption $c_{EF} = 1.1$ leads to a better agreement for H (Table 8).

- Deleted: the sensible heat flux
- Deleted: biases
- Deleted: (Choi et al., 2009).
- Deleted: The same trends observed in the MAD and RMSD values are found in the MRD values presented in Table 7. A striking feature in S1–S3 is the very poor prediction of the sensible heat flux with MRD's between 35 and 47 %. Especially, for S1 and S2 that have been calibrated against ground measured instantaneous latent heat fluxes, this result was not expected. The discrepancy is not caused by any error in the SEBAL procedure but by the apparent bias in the ground measurements of the net radiation that was reported earlier (see Section 4.2). When the ground measured net radiation is replaced with the arguably more accurate SEBAL estimate of net (...)
- Deleted: In Figure 10, the ground measured daily evaporative (...)
- Deleted: 0
- Deleted: 11
- Deleted: 12
- Deleted: , respectively,
- Deleted: sensible
- Deleted: latent
- Deleted: equals
- Deleted: Note there is no need for scenarios
- Deleted: since
- Deleted: net radiations
- Deleted: are very close
- Deleted: equals
- Deleted: is
- Deleted: latent heat fluxes (LE) with a
- Deleted: (=
- Deleted: daily sensible heat fluxes (H) with a
- Deleted: (=
- Deleted: The latter result is another demonstration how the (...)
- Deleted: LE s increase
- Deleted: $(\bar{G} - \bar{S})/\bar{G}$
- Field Code Changed
- Formatted: Font: 12 pt
- Deleted: decrease
- Deleted: improve
- Deleted: a
- Deleted: value of
- Deleted: , although inspection of only the comparison measures in
- Formatted: Font color: Auto
- Deleted: does

1437 Although our results do not suggest with certainty which of the C_{EF} values yields more accurate
1438 estimates of H and LE we recommend the use of 1.1 based on our study (Figure 11), results
1439 reported in the literature (Brutsaert and Sugita, 1992; Anderson et al., 1997), and the improved
1440 daily H fluxes from SEBAL (Table 8).

1441 A comparison between ground measurements and SEBAL estimates of daily
1442 evapotranspiration is shown in Figure 14, Linear relationships between unadjusted EC
1443 measurements of ET and SEBAL estimates of ET based on $C_{EF} = 1.1$ are evident. For scenarios
1444 S1, S2, and S3 the slopes of the relationship varied between 1.32 and 1.08 (mean of 1.23)
1445 suggesting that SEBAL ET estimates were about 21% higher than the unadjusted ET
1446 measurements at the EC towers. This discrepancy is consistent with other studies that reported
1447 systematic underestimation of heat fluxes by the eddy covariance method can be as high as 10 to
1448 30 % (Twine et al., 2000; Paw et al., 2004). Given the inherent uncertainties of the SEBAL
1449 approach and the eddy covariance method the linear relationships between the two methods are
1450 surprisingly good. The SEBAL/METRIC approach is a powerful tool for high resolution
1451 mapping of evapotranspiration even where no meteorological measurements are available on the
1452 ground. This study also demonstrates that the use of SEBAL or METRIC in heterogeneous
1453 landscapes such as arid riparian areas results in ET estimates that are as good as those that could
1454 be obtained using the EC method.

1456 **5. CONCLUSIONS**

1457 We have evaluated the SEBAL extreme-condition-inverse calibration remote sensing
1458 model in arid riparian areas by comparing instantaneous and daily energy balance components

- Deleted: give us
- Deleted: . Nevertheless,
- Deleted: is preferred in our study (non-advective conditions during months April to September) given the regression analysis presented in
- Formatted: Font color: Auto
- Deleted: 10
- Deleted: , data
- Deleted: (Brutsaert and Sugita, 1992; Anderson et al., 1997), and the improved daily sensible heat fluxes by SEBAL in Table 8.
- Deleted: made
- Deleted: 13
- Deleted: where the
- Formatted: Font: Italic
- Deleted: are compared with
- Formatted: Font: Italic
- Deleted: with
- Deleted: of
- Deleted: unadjusted ET measured at the EC tower and the SEBAL estimates are, respectively, 1.30,
- Deleted: ,
- Deleted: which averages to
- Deleted: . Thus,
- Formatted: Font: Italic
- Deleted: are
- Formatted: Font: Italic
- Deleted: expected since it has been reported in the literature that the
- Deleted: (Twine et al., 2000; Paw et al., 2004).
- Deleted: agreement
- Deleted: is
- Deleted: Especially, considering that we compare sensible and latent heat fluxes measured in heterogeneous arid riparian areas. Therefore, this study confirms other studies (Allen et al., 2011; Bastiaanssen et al., 2005) that SEBAL
- Formatted: Font: Italic
- Deleted: In this study we
- Deleted: its predicted

1491 with those measured on the ground with the eddy covariance method.

1492 An analysis of differences in instantaneous R_n during late morning between vegetation
1493 and exposed soil emphasizes the importance of selecting representative soil and vegetative
1494 mixture viewed by the ground R_n sensor. We argue that tower-based R_n is generally biased
1495 toward vegetation, resulting in exaggerated R_n values within the eddy covariance footprint.

1496 Instantaneous R_n from RS, representing a larger area than the net radiometer, systematically gave
1497 lower instantaneous R_n values. When these were used to close the eddy covariance energy
1498 balance, LE and H from SEBAL and ground based eddy covariance were more similar. Daily R_n
1499 values of SEBAL agreed well with the ground measurements. This result can be ascribed to

1500 physical differences between the radiation balance of pixels of mixed riparian vegetation and
1501 bare soil compared to the small footprint of ground R_n sensors placed over vegetation

1502 Instantaneous G values of SEBAL were about 30% higher than the ground measured
1503 values in the San Pedro and Owens Valley. However, this large relative difference had a
1504 relatively minor impact on the overall energy balance because the actual deviation in G was
1505 approximately 5-6% of the SEBAL and ground measured instantaneous R_n . Also, daily G is near

1506 zero because heat enters the soil during the day and exits the soil during the night. In the
1507 application of SEBAL and METRIC for estimating daily ET , it is reasonable to assume G is
1508 negligible.

1509 Instantaneous LE values derived from SEBAL were within -13.2 to 2.7% of the ground
1510 measurements for five different comparisons (scenarios S1-S5). The magnitude of these
1511 differences was similar to the variability common to eddy covariance flux measurements, i.e. it
1512 was not possible in this study of heterogeneous arid riparian areas to determine conclusively

Deleted: (Landsat overpass time)

Deleted: large impact of soil in the R_n view, and the

Deleted: proper

Deleted: higher

Deleted: .

Deleted: SEBAL

Deleted: for heterogeneous vegetation

Deleted: gives

Deleted: are

Deleted: LE and H from the

Deleted: EC are much

Deleted: The daily net radiation

Deleted: agree

Deleted: (Table 4 and Figure 5) as expected after examination of the daily

Formatted: Font color: Text 1

Deleted: pixels in section [4.2].
The instantaneous

Formatted: Font color: Text 1

Formatted: Font color: Text 1

Formatted: Font color: Text 1

Deleted: heat flux

Deleted: Valleys (Table 6 and Figure 6).

Deleted: has

Deleted: since its MAD of 35 W/m² (Table 6) hovers around 6% percent

Deleted: predicted instantaneous net radiation and around 5% percent of the

Formatted: Font: Italic

Deleted: net radiation. The

Deleted: close to

Deleted: since

Deleted: but leaves

Deleted: (Table 6). Therefore

Deleted: can be assumed in SEBAL that the daily heat flux

Deleted: zero.

Deleted: The instantaneous latent heat flux

Deleted: of

Deleted: the

Deleted: (Table 7 and Figure 9).

Deleted: is

Deleted: it is nearly impossible to decide

1550 whether the difference between methods was a result of bias in SEBAL or the eddy covariance
 1551 method. Instantaneous H values of SEBAL differed from the ground measurements by 35.0 to
 1552 47.2%. These H fluxes are necessarily biased because errors in R_n and G are lumped into H as a
 1553 result of the extreme-condition-inverse internal calibration procedure. Substitution of the ground
 1554 measured R_n for the SEBAL R_n in the ground based energy balance improved the comparison
 1555 with the RS-based H with relative differences of only 0.8% and 16.6%. Using a combination of
 1556 ground measured G and H with RS-based R_n yielded the least biased energy balances over
 1557 heterogeneous arid riparian areas.
 1558 Daily H and LE fluxes estimated by SEBAL generally agreed with ground measurements
 1559 (mean MRD'S 13.8 to -0.7%). Better agreement at the daily scale was largely due to the better
 1560 correspondence in daily rather than instantaneous R_n estimates between SEBAL and ground
 1561 measurements. The use of a multiplier on the instantaneous evaporative fraction of 1.1 to convert
 1562 the instantaneous ET to daily ET was preferable for the non-advective conditions during the
 1563 months April to September.
 1564 The instantaneous SEBAL H is intentionally biased during calibration and expected to
 1565 deviate from the ground measured H in order to provide an unbiased estimate of LE . For all five
 1566 calibration scenarios, the comparison measures (r^2 , MAD, RMSD and MRD) of the
 1567 instantaneous and daily LE fluxes were strong evidence that the great strength of the SEBAL and
 1568 METRIC method is their internal calibration procedure that eliminates most of the error in LE
 1569 flux at the expense of increased error in instantaneous H flux. We conclude that the SEBAL
 1570 method is an effective tool for mapping actual evapotranspiration at high spatial resolution in

- Deleted: these differences are
- Deleted: Therefore, we conclude that the SEBAL latent heat fluxes in this study over heterogeneous arid riparian areas are similar to the ones measured at the eddy covariance towers.
- Deleted: The instantaneous sensible heat flux
- Deleted: differ
- Deleted: % in scenarios S1, S2 and S3 but after replacing the
- Deleted: ground measurement of net radiation by the SEBAL net radiation the differences reduce to 0.8% and 16.6% for, respectively, scenarios S4 and S5. As has been explained in section [4.4.1] the SEBAL sensible heat fluxes are biased since
- Deleted: of SEBAL the sensible heat flux absorbs all biases that may occur during the SEBAL implementation.
- Deleted: ¶ In terms of daily sensible
- Deleted: latent heat
- Deleted: , better agreement exists between
- Deleted: and SEBAL estimates with
- Deleted: MRD's for the three scenarios range from
- Deleted: % . That is because
- Deleted: net radiations measured on the
- Deleted: and determined by SEBAL agree well (Table 8 and Figures 11 and 12). Note that the
- Deleted: is preferred
- Deleted: that were covered during this study
- Deleted: An important conclusion of the comparisons between various calibration strategies for
- Formatted: Indent: First line: 0.49", No widow/orphan control, Don't adjust space between Latin and Asian text, Don't adjust space between Asian text and numbers
- Deleted: is that ground measurements of sensible heat fluxes should be used with caution for the calibration and validation of ...
- Deleted: (to produce an unbiased LE) and will
- Deleted: sensible heat flux
- Deleted: arrive at
- Deleted: estimates
- Deleted: ¶
- Deleted: latent heat
- Deleted: are
- Deleted: its
- Deleted: bias
- Deleted: latent heat
- Deleted: bias
- Deleted: sensible heat
- Deleted: resolutions

1617 heterogeneous riparian areas where hourly weather data are unavailable.

Deleted: no high-quality

Deleted: available

1618

1619

ACKNOWLEDGEMENT

1620

The following sponsors have contributed to this study: NSF EPSCoR grant EPS-

1621

0447691; U.S. Department of Agriculture, CSREES grant No.: 2003-35102-13654; New Mexico

1622

Universities Collaborative Research (NUCOR) program for joint research with the Los Alamos

1623

National Laboratory; and NASA New Investigator Program. The energy balance data from

1624

towers in the Middle Rio Grande Valley were provided by Dr. James Cleverly of the University

1625

of New Mexico. We did our own energy balance adjustment.

1626

1627

REFERENCES

1628

Allen, R. G., Pereira, L. S., Raes, D., and Smith, M.: Crop evapotranspiration, FAO Irrigation and drainage paper 56, FAO. Rome, 1998.

1630

Allen, R. G., Tasumi, M., and Trezza, R.: METRICtm Mapping Evapotranspiration at High Resolution.

1631

Applications Manual for Landsat Satellite Imagery. Version 2.0, University of Idaho, Kimberly, Idaho, 139, 2005.

1632

Allen, R. G., Tasumi, M., and Trezza, R.: Benefits from tying satellite-based energy balance to reference

1633

evapotranspiration, Earth Observation for Vegetation Monitoring and Water Management. AIP Conference

1634

Proceedings, 852, 127-137, 2006.

1635

Allen, R. G., Tasumi, M., and Trezza, R.: Satellite-based Energy Balance for Mapping Evapotranspiration with

1636

Internalized Calibration (METRIC) – Model, Journal of Irrigation and Drainage Engineering, 133, 380-394, 2007.

1637

Allen, R. G., Irmak, A., Trezza, R., Hendrickx, J. M. H., Bastiaanssen, W. G. M., and Kjaersgaard, J.: Satellite-based

1638

ET estimation in agriculture using SEBAL and METRIC, Hydrologic Processes, 25, 4011-4027, 2011.

1639

Anderson, M. C., Norman, J. M., Diak, G. R., Kustas, W. P., and Mecikalski, J. R.: A two-source time-integrated

1640

model for estimating surface fluxes using thermal infrared remote sensing, Remote Sensing of Environment, 60,

1641

195-216, 1997.

1642

Arya, P. S.: Introduction to micrometeorology, Academic press, 2001.

1643

Bastiaanssen, W. G. M.: Regionalization of surface flux densities and moisture indicators in composite terrain: a

1644

remote sensing approach under clear skies in Mediterranean climates, Landbouwniversiteit te Wageningen, 1995.

1645

Bastiaanssen, W. G. M., Menenti, M., Feddes, R. A., and Holtslag, A. A. M.: A remote sensing surface energy

1646

balance algorithm for land (SEBAL). Part 1: Formulation, Journal of Hydrology, 212-213, 198-212, 1998a.

1647

Bastiaanssen, W. G. M., Pelgrum, H., Wang, J., Ma, Y., Moreno, J. F., Roerink, G. J., Roebeling, R. A., and Wal, T. v.

1648

d.: A remote sensing surface energy balance algorithm for land (SEBAL). Part 2: Validation, Journal of Hydrology,

1649

212-213, 213-229, 1998b.

1650

Bastiaanssen, W. G. M.: SEBAL-based sensible and latent heat fluxes in the Irrigated Gediz Basin, Turkey, Journal

1651

of Hydrology, 229, 87-100, 2000.

1652

Bastiaanssen, W. G. M., Ahmad, M.-D., and Chemin, Y.: Satellite surveillance of evaporative depletion across the

1653

Indus Basin, Water Resources Research, 38, 1273, doi:10.1029/2001WR000386, 2002.

1656 Bastiaanssen, W. G. M., Noordman, E. J. M., Pelgrum, H., Davids, G., Thoreson, B. P., and Allen, R. G.: SEBAL
1657 model with remotely sensed data to improve water-resources management under actual field conditions, *Journal of*
1658 *Irrigation and Drainage Engineering*, 131, 85-93, 2005.

1659 Bastiaanssen, W. G. M., Klaasse, A., Zwart, S., Immerzeel, W., and Droogers, P.: The hydrological flow path and
1660 options for sustainable water resources management in the overexploited Rio Bravo Basin, A world bank project,
1661 Final report, 102p, 2006.

1662 Brutsaert, W., and Sugita, M.: Application of self-preservation in the diurnal evolution of the surface energy budget
1663 to determine daily evaporation, *Journal of Geophysical Research*, 97, 18,377-318,382, 1992.

1664 Brutsaert, W., Hsu, A. Y., and Schmugge, T. J.: Parameterization of surface heat fluxes above a forest with satellite
1665 thermal sensing and boundary layer soundings, *Journal of Applied Meteorology*, 32, 909-917, 1993.

1666 Choi, M., Kustas, W. P., Anderson, M. C., Allen, R. G., Li, F., and Kjaersgaard, J. H.: An intercomparison of three
1667 remote sensing-based surface energy balance algorithms over a corn and soybean production region (Iowa, US)
1668 during SMACEX, *Agricultural and Forest Meteorology*, 149, 2082-2097, 2009.

1669 Choudhury, B. J.: Estimating evaporation and carbon assimilation using infrared temperature data: vistas in
1670 modeling, Theory and Application of Remote Sensing, edited by: Asrar, G., Wiley, New York, 628-690 pp., 1989.

1671 Cleverly, J. R., Dahm, C. N., Thibault, J. R., Gilroy, D. J., and Coonrod, J. E. A.: Seasonal estimates of actual evapo-
1672 transpiration from Tamarix ramosissima stands using three-dimensional eddy covariance, *Journal of Arid*
1673 *Environments*, 52, 181-197 doi:10.1006/jare.2002.0972, 2002.

1674 Compaoré, H., Hendrickx, J. M. H., Hong, S.-h., Friesen, J., van de Giesen, N. C., Rodgers, C., Szarzynski, J., and
1675 Vlek, P. L. G.: Evaporation mapping at two scales using optical imagery in the White Volta Basin, Upper East Ghana
1676 *Physics and Chemistry of the Earth, Parts A/B/C*, 33, 127-140, doi:10.1016/j.pce.2007.1004.1021, 2008.

1677 Costigan, K. R., Bossert, J. E., and Langley, D. L.: Atmospheric/hydrologic models for the Rio Grande Basin:
1678 simulations of precipitation variability, *Global and Planetary Change*, 25, 83-110, 2000.

1679 Crago, R. D.: Conservation and variability of the evaporative fraction during the daytime, *Journal of Hydrology*, 180,
1680 173-194, 1996.

1681 De Bruin, H. A. R.: In: J.C Hooghart (Ed.), From Penman to Makkink, Evaporation and weather. Proceedings and
1682 Information No. 39, TNO Committee on Hydrological Research, The Hague, pp. 5-31., 1987.

1683 De Bruin, H. A. R., Bink, N. J., and Kroon, L. J. M.: Fluxes in the surface layer under advective conditions, *Land*
1684 *surface evaporation*, edited by: Schmugge, T. J., and Andre, J.-C., Springer-Verlag New York, Inc., 1991.

1685 Droogers, P., and Allen, R. G.: Estimating reference evapotranspiration under inaccurate data conditions, *Irrigation*
1686 *and Drainage Systems*, 16, 33-45, 2002.

1687 Du, J., Song, K., Wang, Z., Zhang, B., and Liu, D.: Evapotranspiration Estimation Based on MODIS Products and
1688 Surface Energy Balance Algorithms for Land (SEBAL) Model in Sanjiang Plain, Northeast China., *Chinese*
1689 *Geographical Science*, 23, 73-91, 2013.

1690 Elmore, A. J., Mustard, J. F., and Manning, S. J.: Regional patterns of plant community response to changes in water:
1691 Owens Valley, California., *Ecological Applications*, 13, 443-460, 2002.

1692 Farah, H. O., Bastiaanssen, W. G. M., and Feddes, R. A.: Evaluation of the temporal variability of the evaporative
1693 fraction in a tropical watershed, *International Journal of Applied Earth Observation and Geoinformation* 5, 129-140,
1694 2004.

1695 Field, R. T., Fritschen, L. J., Kanemasu, E. T., Smith, E. A., Stewart, J. B., Verma, S. B., and Kustas, W. B.:
1696 Calibration, comparison and correction of net radiation instruments used during FIFE, *Journal of Geophysical*
1697 *Research*, 97, 18681-18695, 1992.

1698 Fox, D. G.: Judging air quality model performance: A summary of the AMS Workshop on Dispersion Model
1699 Performance, *Bulletin of the American Meteorological Society*, 62, 599-609, 1981.

1700 Franks, S. W., and Beven, K. J.: Estimation of evapotranspiration at the landscape scale: a fuzzy disaggregation
1701 approach, *Water Resources Research*, 33, 2929-2938, 1997.

1702 Fuchs, M., and Hadas, A.: Analysis and performance of an improved soil heat flux transducer, *Soil Science Society*
1703 *of America, Proceedings*, 37, 173-175, 1973.

1704 Gibson, L. A., Jarmain, C., Su, Z., and Eckardt, F.: Review: Estimating evapotranspiration using remote sensing and
1705 the Surface Energy Balance System – A South African perspective, *Water SA*, 39, 477-483, 2013.

1706 Granger, R. J.: Satellite-derived estimates of evapotranspiration in the Gediz basin, *Journal of Hydrology*, 229, 70-
1707 76, 2000.

1708 Halldin, S., and Lundroth, A.: Errors in net radiometry: comparison and evaluation of six radiometer designs, *ournal*

1709 of Atmospheric and Oceanic Technology, 16, 762-783, 1992.

1710 Hemakumara, H., Chandrapala, L., and Moene, A.: Evapotranspiration fluxes over mixed vegetation areas measured
1711 from a large aperture scintillometer, *Agricultural Water Management*, 58, 109–122, 2003.

1712 Hendrickx, J. M. H., Vink, N. H., and Fayinke, T.: Water requirement for irrigated rice in a semi-arid region in West
1713 Africa, *Agricultural Water Management*, 11, 75-90, 1986.

1714 Hong, S.-H.: Mapping regional distributions of energy balance components using optical remotely sensed imagery.
1715 Ph.D. Dissertation Thesis, New Mexico Institute of Mining and Technology, Socorro NM, 378 pp., 2008.

1716 Hsieh, C.-L., Katul, G. G., and Chi, T.-W.: An approximate analytical model for footprint estimation of scalar fluxes
1717 in thermally stratified atmospheric flows, *Advances in Water Resources*, 23, 765-772, 2000.

1718 Humes, K. S., Kustas, W. P., Moran, M. S., Nichols, W. D., and Weltz, M. A.: Variability of emissivity and surface
1719 temperature over a sparsely vegetated surface, *Water Resources Research*, 30, 1299-1310, 1994.

1720 Jacob, F., Olioso, A., Gu, X. F., Su, Z., and Seguin, B.: Mapping surface fluxes using airborne visible, near infrared,
1721 thermal infrared remote sensing data and a spatialized surface energy balance model, *Agronomie*, 22, 669–680 669
1722 DOI: 610.1051/agro:2002053, 2002.

1723 Jiang, L., and Islam, S.: Estimation of surface evaporation map over southern Great Plains using remote sensing data,
1724 *Water Resources Research*, 37, 329-340, 2001.

1725 Karimi, P., and Bastiaanssen, W. G. M.: Spatial evapotranspiration, rainfall and land use data in water accounting –
1726 Part 1: Review of the accuracy of the remote sensing data, *Hydrol. Earth Syst. Sci.*, 19, 507-532, 2015.

1727 Kite, G. W., and Droogers, P.: Comparing evapotranspiration estimates from satellites, hydrological models and field
1728 data, *Journal of Hydrology*, 229, 3-18, 2000.

1729 Kizer, M. A., and Elliott, R. L.: Eddy correlation systems for measuring evapotranspiration, *Transactions of*
1730 *American Society of Agricultural Engineers*, 34, 387-392, 1991.

1731 Kleissl, J., Gomez, J. D., Hong, S.-H., and Hendrickx, J. M. H.: Large aperture scintillometer intercomparison study,
1732 *Boundary-Layer Meteorology*, 128, 133-150, 2008.

1733 Kleissl, J., Hong, S.-H., and Hendrickx, J. M. H.: New Mexico scintillometer network. Supporting remote sensing
1734 and hydrologic and meteorological models, *Bulletin American Meteorological Society*, 90, 207-218, 2009.

1735 Kurc, S. A., and Small, E. E.: Dynamics of evapotranspiration in semiarid grassland and shrubland ecosystems
1736 during the summer monsoon season, central New Mexico, *Water Resources Research*, 40, W09305,
1737 doi:09310.01029/02004WR003068, 2004.

1738 Kustas, W. P., and Norman, J. M.: Use of remote sensing for evapotranspiration monitoring over land surfaces,
1739 *Hydrological Sciences Journal*, 41, 495-516, 1996.

1740 Kustas, W. P., Prueger, J. H., Hatfield, J. L., Ramalingam, K., and Hipps, L. E.: Variability in soil heat flux from a
1741 mesquite dune site, *Agricultural and Forest Meteorology*, 103, 249– 264, 2000.

1742 Loescher, H. W., Ocheltree, T., Tanner, B., Swiatek, E., Dano, B., Wong, J., Zimmerman, G., Campbell, J., Stock, C.,
1743 Jacobsen, L., Shiga, Y., Kollas, J., Liburdy, J., and Law, B. E.: Comparison of temperature and wind statistics in
1744 contrasting environments among different sonic anemometer-thermometers, *Agricultural Forest Meteorol.*, 133, 119-
1745 139, 2005.

1746 Ma, Y., Menenti, M., Tsukamoto, O., Ishikawa, H., Wang, J., and Gao, Q.: Remote sensing parameterization of
1747 regional land surface heat fluxes over arid area in northwestern China, *Journal of Arid Environments*, 57, 257-273,
1748 2004.

1749 Moran, M. S., and Jackson, R. B.: Assessing the spatial distribution of evapotranspiration using remotely sensed
1750 inputs, *Journal of Environmental Quality*, 20, 725-735, 1991.

1751 Mu, Q., Zhao, M., and Running, S. W.: Improvements to a MODIS global terrestrial evapotranspiration algorithm,
1752 *Remote Sensing of Environment*, 115, 1781-1800, 2011.

1753 Norman, J. M., Kustas, W. P., and Humes, K. S.: A two-source approach for estimating soil and vegetation energy
1754 fluxes from observations of directional radiometric surface temperature, *Agriculture and Forest Meteorology*, 77,
1755 263-293, 1995.

1756 Norman, J. M., Anderson, M. C., Kustas, W. P., French, A. N., Mecikalski, J., Torn, R., Diak, G. R., Schmugge, T. J.,
1757 and Tanner, B. C. W.: Remote sensing of surface energy fluxes at 10 1-m pixel resolutions, *Water Resources*
1758 *Research*, 39, 1221. doi:1210.1029/2002WR001775., 2003.

1759 Parlange, M. B., Eichinger, W. E., and Albertson, J. D.: Regional scale evaporation and the atmosphere boundary
1760 layer, *Reviews of Geophysics*, 33, 99-124, 1995.

1761 Paw, K. T., Wharton, S., Xu, L., Falk, M., Schroeder, M., and Gonzales, E.: Zen and the art of energy balance

1762 closure, Symposium "Progress in Radiation and Energy Balance Closure", 68th Annual Meeting Soil Science
1763 Society of America, Seattle, Washington, 2004.

1764 Pelgrum, H., and Bastiaanssen, W. G. M.: An intercomparison of techniques to determine the area-averaged latent
1765 heat flux from individual in situ observations: a remote sensing approach using the European Field Experiment in a
1766 Desertification-Threatened Area data, *Water Resources Research*, 32, 2775–2786, 1996.

1767 Sauer, T. J.: Soil Heat Flux. *Encyclopedia of Soil Science*, edited by: Lal, R., Marcel Dekker, INC., New York, NY,
1768 647-649 pp., 2002a.

1769 Sauer, T. J.: Heat flux density, in: *Methods of soil analysis. Part 1*, edited by: Dane, J., and Topp, C., Soil Science
1770 Society of America Madison, Wisconsin, 1233-1248, 2002b.

1771 Sauer, T. J., Meek, D. W., Ochsner, T. E., Harris, A. R., and Horton, R.: Errors in heat flux measurement by flux
1772 plates of contrasting design and thermal conductivity, *Vadose Zone Journal*, 2, 580-588, 2003.

1773 Schmid, H. P., and Oke, T. R.: A model to estimation the source area contributing to turbulent exchange in the
1774 surface layer over patchy terrain, *Quarterly Journal of The Royal Meteorological Society*, 116, 965-988, 1990.

1775 Schuepp, P. H., Leclerc, M. Y., MacPherson, J. I., and Desjardins, R. L.: Footprint prediction of scalar fluxes from
1776 analytical solutions of the diffusion equation, *Boundary-Layer Meteorology*, 50, 355-373, 1990.

1777 Schüttemeyer, D., Schillings, C., Moene, A. F., and Bruin, H. A. R. D.: Satellite-based actual evapotranspiration over
1778 drying semiarid terrain in West Africa, *Journal of Applied Meteorology and Climatology*, 46, 97-111 DOI:
1779 10.1175/JAM2444.1171, 2007.

1780 Scott, R. L., Shuttleworth, J. W., Goodrich, D. C., and Maddock III, T.: The water use of two dominant vegetation
1781 communities in a semiarid riparian ecosystem, *Agricultural and Forest Meteorology*, 105, 241-256, 2000.

1782 Scott, R. L., Edwards, E. A., Shuttleworth, W. J., Huxman, T. E., Watts, C., and Goodrich, D. C.: Interannual and
1783 seasonal variation in fluxes of water and carbon dioxide from a riparian woodland ecosystem, *Agricultural and
1784 Forest Meteorology*, 122, 65–84, 2004.

1785 Seguin, B. D., and Itier, B.: Using midday surface temperature to estimate daily evapotranspiration from satellite
1786 thermal IR data, *International Journal of Remote Sensing*, 4, 371-383, 1983.

1787 Senay, G. B., Bohms, S., Singh, R. K., Gowda, P. H., Velpuri, N. M., Alemu, H., and Verdin, J. P.: Operational
1788 evapotranspiration mapping using remote sensing and weather datasets: A new parameterization for the SSEB
1789 approach, *JAWRA Journal of the American Water Resources Association*, 49, 577-591, 2013.

1790 Steinwand, A. L., Harrington, R. F., and Or, D., 2006.: Water balance for Great Basin phreatophytes derived from
1791 eddy covariance, soil water, and water table measurements, *Journal of Hydrology*, 329, 595-605, 2006.

1792 Stromberg, J. C.: Dynamics of Fremont cottonwood (*Populus fremontii*) and saltcedar (*Tamarix chinensis*)
1793 populations along the San Pedro River, Arizona, *Journal of Arid Environments*, 40, 133-155, 1998.

1794 Su, Z.: The Surface Energy Balance System (SEBS) for estimation of turbulent heat fluxes, *Hydrology and Earth
1795 System Sciences*, 6, 85-99, 2002.

1796 Sugita, M., and Brutsaert, W.: Daily evaporation over a region from lower boundary layer profiles measured with
1797 radiosondes, *Water Resources Research*, 27, 747-752, 1991.

1798 Tasumi, M.: Progress in operational estimation of regional evapotranspiration using satellite imagery, Ph.D. Thesis,
1799 University of Idaho, Moscow, Idaho, 2003.

1800 Teixeira, A. H. d. C., Bastiaanssen, W. G. M., Moura, M. S. B., Soares, J. M., Ahmad, M. D., and Bos, M. G.:
1801 Energy and water balance measurements for water productivity analysis in irrigated mango trees, Northeast Brazil,
1802 *Agricultural and Forest Meteorology*, 148, 1524-1537, 2008.

1803 Trezza, R.: Evapotranspiration using a satellite-based surface energy balance with standardized ground control. Ph.D.
1804 Thesis, Utah State University: Logan, Utah., 2002.

1805 Twine, T. E., Kustas, W. P., Norman, J. M., Cook, D. R., Houser, P. R., Meyers, T. P., Prueger, J. H., Starks, P. J., and
1806 Wesely, M. L.: Correcting eddy-covariance flux underestimates over a grassland, *Agricultural and Forest
1807 Meteorology*, 103, 279-300, 2000.

1808 Wang, J., Bastiaanssen, W. G. M., Ma, Y., and Pelgrum, H.: Aggregation of land surface parameters in the oasis-
1809 desert systems of Northwest China, *Hydrological Sciences*, 12, 2133-2147, 1998.

1810 Willmott, C. J., and Wicks, D. E.: An empirical method for the spatial interpolation of monthly precipitation within
1811 California, *Physical Geography*, 1, 59-73, 1980.

1812 Willmott, C. J.: On the validation of models, *Physical Geography*, 2, 184-194, 1981.

1813 Willmott, C. J.: Some comments on the evaluation of model performance, *Bulletin of the American Meteorological
1814 Society*, 63, 1309–1313, 1982.

1815 Wilson, K., Goldstein, A., Falge, E., Aubinet, M., Baldocchi, D., Berbigier, P., Bernhofer, C., Ceulemans, R.,
1816 Dolman, H., Field, C., Grelle, A., Ibrom, A., Law, B. E., Kowalski, A., Meyers, T., Moncrieff, J., Monson, R.,
1817 Oechel, W., Tenhunen, J., Valentini, R., and Verma, S.: Energy balance closure at FLUXNET sites, *Agric. For.*
1818 *Meteorol.*, 113, 223-243, 2002.
1819 Wright, J. L.: New evapotranspiration crop coefficients, *Journal of Irrigation and Drainage Engineering*, 108, 57-74,
1820 1982.
1821 Yang, Y. T., and Shang, S. H.: A hybrid dual source scheme and trapezoid framework based evapotranspiration
1822 model (HTEM) using satellite images: algorithm and model test, *Journal of Geophysical Research*, 118, 2284-2300,
1823 2013.
1824 Zwart, S. J., and Leclert, L. M. C.: A remote sensing-based irrigation performance assessment: a case study of the
1825 Office du Niger in Mali, *Irrigation science*, 28, 371-385, 2010.
1826
1827

1828 **Table 1.** List of Landsat 7 ETM+ images used in this study (overpass around 10:30 am).
1829

Area	Date	Path/Row
Rio Grande	04/07/2000	33/36
Rio Grande	07/28/2000	33/36
Rio Grande	09/14/2000	33/36
Rio Grande	09/30/2000	33/36
Rio Grande	05/09/2000	33/36
Rio Grande	06/04/2001	34/36
Rio Grande	05/06/2002	34/36
Rio Grande	05/31/2002	33/36
Rio Grande	05/31/2002	33/37
Rio Grande	06/16/2002	33/36
Rio Grande	08/19/2002	33/36
Owens Valley	07/10/2002	41/34
Owens Valley	08/11/2002	41/34
Owens Valley	09/12/2002	41/34
San Pedro	05/16/2003	35/38
San Pedro	08/12/2003	35/38

1830
1831
1832
1833
1834
1835
1836

1837 **Table 2.** Site characteristics and sensor heights on the eddy covariance towers.
 1838

Site	Longitude/ Latitude	Vegetation type	Elevation (m)	Vegetation height (m)	Sensor height (m)
Rio Grande – BDAS	106.88W/ 33.78 N	saltcedar	1370	6.2	8.2
Rio Grande – BLN	106.75W/ 34.59N	cottonwood	1460	25.1	27.2
Rio Grande – SEV	106.87W/ 34.27N	saltcedar	1430	4.9	6.5
Rio Grande – SHK	106.68W/ 34.96N	cottonwood	1500	23.7	26.3
Owens – FSL138	118.43W/ 37.41N	alkali meadow	1280	0.2	2.5
Owens – PLC018	118.35W/ 37.37N	rabbitbrush scrub	1250	0.5	2.5
Owens – PLC074	118.36W/ 37.32N	saltbush meadow	1240	1.0	2.5
Owens – PLC185	118.33W/ 37.27N	desert sink scrub	1220	0.5	2.5
Owens – BLK100	118.24W/ 36.90N	alkali meadow	1170	0.2	2.5
San Pedro – CM	110.18W/ 31.66N	mesquite	1190	7.0	14
San Pedro – LSS	110.14W/ 31.56N	sacaton	1230	1.0	3.5
San Pedro – LSM	110.13W/ 31.57N	mesquite	1240	3.5	6.5

1839
 1840
 1841
 1842
 1843
 1844
 1845

1846 **Table 3.** Scenarios of comparison between RS-based estimates and ground measurements of net
 1847 radiation R_n , soil heat flux G , and sensible and latent heat fluxes H and LE .
 1848

Deleted: SEBAL

ID	Scenario	R_n Used for Energy Balance Closure
S1	EC Approach (EC_FP) ¹	Ground Measured R_n
S2	EC Approach (EC_TP) ²	Ground Measured R_n
S3	EM Approach ³	Ground Measured R_n
S4	EC Approach (EC_TP/SR _n) ⁴	<u>RS</u> Estimated R_n
S5	EM Approach (SR _n) ⁵	<u>RS</u> Estimated R_n

Deleted: SEBAL

Deleted: SEBAL

1850
 1851 ¹Hot pixel selected by matching the ground measured instantaneous LE (adjusted for closure error using the ground
 1852 measured R_n) at satellite overpass with the footprint weighted averaged SEBAL LE . SEBAL LE compared against
 1853 ground measured instantaneous LE (adjusted for closure error using the ground measured R_n) at satellite overpass.
 1854 ²Hot pixel selected by matching the ground measured instantaneous LE (adjusted for closure error using the ground
 1855 measured R_n) at satellite overpass with the SEBAL LE at the tower pixel. SEBAL LE compared against ground
 1856 measured instantaneous LE (adjusted for closure error using the ground measured R_n) at satellite overpass.
 1857 ³Hot pixel selected by the empirical approach without use of ground measurements. SEBAL LE is compared against
 1858 ground measured instantaneous LE (adjusted for closure error using the ground measured R_n) at satellite overpass.
 1859 ⁴Hot pixel selected by matching the ground measured instantaneous LE (adjusted for closure error using the ground
 1860 measured R_n) at satellite overpass with the SEBAL LE at the tower pixel. SEBAL LE compared against ground
 1861 measured instantaneous LE (adjusted for closure error using the SEBAL estimated R_n) at satellite overpass.
 1862 ⁵Hot pixel selected by the empirical approach without use of ground measurements. SEBAL LE is compared against
 1863 ground measured instantaneous LE (adjusted for closure error using the SEBAL estimated R_n) at satellite overpass.

1867 **Table 4.** Quantitative measures for comparison of **RS-based** instantaneous and daily net radiation
 1868 estimates (\bar{S}) versus ground measurements (\bar{G}) using the EC and Empirical Approaches for
 1869 selection of hot and cold pixels.
 1870

Selection Cold and Hot Pixel	n	\bar{G}	\bar{S}^4	SD_G	SD_S	r^2	MAD	RMSD	MI
Instantaneous R_n									
	(-)	(W/m ²)	(W/m ²)	(W/m ²)	(W/m ²)	(-)	(W/m ²)	(W/m ²)	
S1 - EC Approach (FP ¹)	25	654	569	86	90	0.56	88	105	11
S2 - EC Approach (TP ²)	25	654	571	86	89	0.56	87	103	12
S3 - Empirical Approach	25	654	559	86	88	0.56	97	113	14
Daily R_n									
	(-)	(MJ/m ² /d)	(MJ/m ² /d)	(MJ/m ² /d)	(MJ/m ² /d)	(-)	(MJ/m ² /d)	(MJ/m ² /d)	%
S1/S2 - EC Approach ³	24	15.6	16.0	3.1	3.1	0.75	1.3	1.6	-2.9
S3 - Empirical Approach	24	15.6	15.9	3.1	3.0	0.69	1.3	1.8	-2.3

1871
 1872 ¹Cold and hot pixels were selected by matching the instantaneous *LE* measured at the EC tower with the footprint
 1873 weighted averaged SEBAL instantaneous *LE*. ²Cold and hot pixels were selected by matching the instantaneous *LE*
 1874 measured at the EC tower with the SEBAL instantaneous *LE* of the EC tower pixel. ³The daily R_n does not depend
 1875 on the selection of the cold and hot pixels; both EC Approaches yield the same values. ⁴The SEBAL instantaneous
 1876 R_n estimate (\bar{S}) was obtained by calculating the footprint weighted average for the instantaneous R_n ; the daily R_n
 1877 (\bar{S}) was obtained as the average SEBAL daily R_n of the 25 pixels around the EC tower.
 1878

Deleted: SEBAL

Deleted: \bar{S}

Deleted: \bar{G}

Formatted: Font: Not Italic

Formatted: Font: Not Italic

Field Code Changed

Deleted: \bar{G}

Field Code Changed

Deleted: \bar{S}^4

Field Code Changed

Deleted: \bar{S}

Field Code Changed

Deleted: \bar{S}

Field Code Changed

1886 **Table 5.** Selected instantaneous and daily net radiation fluxes and relevant parameters for
 1887 adjacent clusters of vegetated and bare soil pixels on June 16, 2002.
 1888

Vegetation	Albedo (-)		NDVI ¹ (-)		T-surface (degree K)		Instantaneous Net Radiation (W/m ²)			Daily Net Radiation (MJ/(m ² d))			N ²
	Veg	Bare	Veg	Bare	Veg	Bare	Veg	Bare	Ratio	Veg	Bare	Ratio	
Alfalfa	0.22	0.32	0.84	0.14	299	325	634	384	1.65	17.9	14.8	1.21	50
Alfalfa	0.21	0.31	0.80	0.24	301	322	627	408	1.54	18.1	15.1	1.20	20
saltcedar	0.16	0.32	0.65	0.14	302	326	670	379	1.77	19.8	14.8	1.34	50
saltcedar	0.14	0.31	0.49	0.24	308	322	657	408	1.61	20.6	15.1	1.36	20

1889

1890 ¹NDVI = Normalized Difference Vegetation Index, ²N = number of pixels in each

1891 **Table 6.** Quantitative measures for comparison of instantaneous and daily RS-based soil heat flux estimates (\bar{S}) versus ground
 1892 measurements (\bar{G}) using the EC and Empirical Approaches for selection of hot and cold pixels.

Selection Cold and Hot Pixel	N ⁴	\bar{G}	\bar{S} ⁵	SD_G	SD_S	r ²	MAD	RMSD	MRD
Instantaneous G	(-)	(W/m ²)	(W/m ²)	(W/m ²)	(W/m ²)	(-)	(W/m ²)	(W/m ²)	%
EC Approach (FP ¹)	6	76	101	26	13	0.02	35	35	-32.2
EC Approach (TP ²)	6	76	101	26	13	0.02	35	35	-31.9
Empirical Approach	6	76	100	26	13	0.02	34	34	-30.9
Daily G	(-)	(MJ/m ² /d)	(MJ/m ² /d)	(MJ/m ² /d)	(MJ/m ² /d)	(-)	(MJ/m ² /d)	(MJ/m ² /d)	%
EC Approach ³	24	0.5	0.0	0.4	0.0	-	0.5	0.6	>100
Empirical Approach	24	0.5	0.0	0.4	0.0	-	0.5	0.6	>100

1894
 1895 ¹ Cold and hot pixels were selected by matching the instantaneous *LE* measured at the EC tower with the footprint weighted averaged SEBAL
 1896 instantaneous *LE*. ² Cold and hot pixels were selected by matching the instantaneous *LE* measured at the EC tower with the SEBAL instantaneous *LE* of
 1897 the EC tower pixel. ³ The daily soil heat flux does not depend on the selection of the cold and hot pixels; both EC Approaches yield the same values.
 1898 ⁴ No instantaneous soil heat flux measurements were available in the Middle Rio Grande Basin. ⁵ The RS-based instantaneous soil heat flux estimate (\bar{S})
 1899 was obtained by calculating the footprint average for the instantaneous soil heat flux; the daily soil heat flux (\bar{S}) was obtained as the average SEBAL
 1900 daily soil heat flux of the 25 pixels around the EC tow.

Deleted: SEBAL
 Deleted: \bar{S}
 Field Code Changed
 Deleted: \bar{G}
 Formatted: Font: Not Italic
 Formatted: Font: Not Italic
 Deleted: \bar{G}
 Field Code Changed
 Deleted: \bar{S} ⁵
 Field Code Changed

Deleted: SEBAL
 Deleted: \bar{S}
 Field Code Changed
 Deleted: \bar{S}
 Field Code Changed

1909 **Table 7.** Quantitative measures for comparison of SEBAL derived instantaneous sensible (H) and latent (LE) heat fluxes
 1910 estimates (\bar{S}) versus ground measurements (\bar{G}).

Scenario	Selection Anchor Pixel	Comments	n	\bar{G}		\bar{S}		SD_G	SD_S	r^2	MAD	RMSD	MRD
				(-)	(W/m ²)	(W/m ²)	(W/m ²)						
S1	EC Approach (FP) ¹	-	H	25	262	156	151	105	0.76	108	131	40.4	
			LE	25	299	314	174	170	0.90	39	57	-5.0	
S2	EC Approach (TP) ²	-	H	25	262	138	151	91	0.81	126	147	47.2	
			LE	25	299	333	174	162	0.85	56	74	-11.5	
S3	EM Approach	-	H	25	262	171	151	77	0.64	111	135	35.0	
			LE	25	299	291	174	143	0.78	66	81	2.7	
S4	EC Approach (TP) ³	SEBAL R_n replaces ground R_n ⁴	H	25	209	207	112	114	0.83	36	46	0.8	
			LE	25	262	258	171	170	0.92	39	48	1.7	
S5	EM Approach	SEBAL R_n replaces ground R_n ⁵	H	25	205	171	110	77	0.59	61	77	16.6	
			LE	25	257	291	167	143	0.82	61	77	-13.2	

1911
 1912 ¹ Anchor pixels were selected by matching the instantaneous LE at the satellite overpass measured at the EC tower and the footprint weighted averaged
 1913 SEBAL flux. ² Anchor pixels were selected by matching the instantaneous LE at the satellite overpass measured at the EC tower and the SEBAL flux of
 1914 the tower pixel. ³ Anchor pixels were selected by matching the instantaneous LE at the satellite overpass measured at the EC tower and the SEBAL flux
 1915 of the tower pixel. In S4, the SEBAL estimated R_n replaces the R_n measured on the ground for adjustment of the latent heat flux. ⁴ Instead of using the R_n
 1916 measurements made on the ground, the SEBAL derived R_n in Scenario 2 is used for the determination of the ground measured energy balance and in
 1917 adjusting the H and LE from the EC for closure error (using Bowen ratio). ⁵ Instead of using the R_n measurements made on the ground, the SEBAL
 1918 derived R_n in Scenario 3 is used for the determination of the ground measured energy balance and in adjusting the H and LE from the EC for closure
 1919 error (using Bowen ratio). ⁶ The heat fluxes have been calculated from the EC measurements. Since no soil heat flux measurements were available for
 1920 the Middle Rio Grande Basin, the SEBAL soil heat flux was used to establish the ground measured energy balance. ⁷ The SEBAL estimates of the
 1921 instantaneous H and LE were obtained by calculating the footprint weighted averaged SEBAL heat fluxes.
 1922

Deleted: \bar{S}

Field Code Changed

Deleted: \bar{G}

Deleted: \bar{G}_s

Field Code Changed

Deleted: \bar{S}^7

Field Code Changed

1927
1928
1929
1930
1931

Table 8. Quantitative measures for comparison of SEBAL derived daily sensible (H) and latent (LE) heat fluxes estimates (\overline{S}) versus ground measurements (\overline{G}).

$EF_{24} = 1.0 \times EF_{inst}$

Scenario	Selection Anchor Pixel	n	(-)	\overline{G}	\overline{S}	SD_G	SD_S	r^2	MAD	RMSD	MRD
				MJ/(m ² d)	MJ/(m ² d)	MJ/(m ² d)	MJ/(m ² d)	(-)	MJ/(m ² d)	MJ/(m ² d)	%
S1	EC Approach (FP) ¹	H	24	6.0	7.2	3.7	3.2	0.41	2.3	3.1	-19.4
		LE	24	9.1	8.9	4.4	4.9	0.78	1.7	2.2	2.9
S2	EC Approach (TP) ²	H	24	6.0	6.9	3.7	3.3	0.32	2.6	3.3	-14.9
		LE	24	9.1	9.1	4.4	5.0	0.72	2.2	2.6	0.0
S3	EM Approach	H	24	6.0	7.6	3.7	2.7	0.37	2.6	3.3	-27.0
		LE	24	9.1	8.3	4.4	4.2	0.69	1.9	2.6	8.9

1932
1933
1934

$EF_{24} = 1.1 \times EF_{inst}$

Scenario	Selection Anchor Pixel	n	(-)	\overline{G}	\overline{S}	SD_G	SD_S	r^2	MAD	RMSD	MRD
				MJ/(m ² d)	MJ/(m ² d)	MJ/(m ² d)	MJ/(m ² d)	(-)	MJ/(m ² d)	MJ/(m ² d)	%
S1	EC Approach (FP) ¹	H	24	6.0	6.3	3.7	3.5	0.41	2.1	3.0	-5.6
		LE	24	9.1	9.7	4.4	5.3	0.78	1.9	2.5	-6.3
S2	EC Approach (TP) ²	H	24	6.0	6.0	3.7	3.6	0.32	2.7	3.3	-0.8
		LE	24	9.1	10.0	4.4	5.4	0.71	2.4	3.0	-9.3
S3	EM Approach	H	24	6.0	6.9	3.7	3.0	0.42	2.3	2.9	-14.8
		LE	24	9.1	9.2	4.4	4.6	0.69	2.0	2.5	-0.3

1935
1936
1937
1938
1939
1940
1941

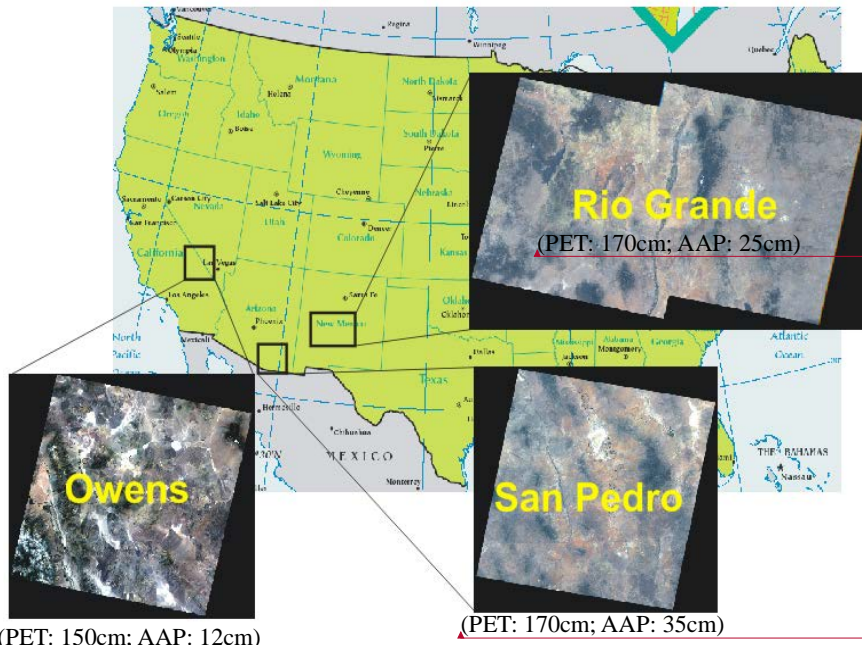
¹ Anchor pixels were selected by matching the instantaneous LE at the satellite overpass measured at the EC tower and the footprint weighted averaged SEBAL flux. ² Anchor pixels were selected by matching the instantaneous LE at the satellite overpass measured at the EC tower and the SEBAL flux of the tower pixel. ⁵ Instead of using the R_n measurements made on the ground, the SEBAL derived R_n in Scenario 3 is used for the determination of the ground measured energy balance. ⁶ The heat fluxes have been calculated from the EC measurements. Since no soil heat flux measurements were available for the Middle Rio Grande Basin, the SEBAL soil heat flux was used to establish the ground measured energy balance. ⁷ The SEBAL estimates of the instantaneous H and LE were obtained by calculating the footprint weighted averaged SEBAL heat fluxes.

Deleted: \overline{S}
Field Code Changed
Deleted: \overline{G}

Deleted: \overline{G}
Field Code Changed
Deleted: \overline{S}
Field Code Changed

Deleted: \overline{G}
Field Code Changed
Deleted: \overline{S}
Field Code Changed

1948
1949
1950
1951
1952
1953
1954
1955
1956



Formatted: Font: (Default) Times New Roman

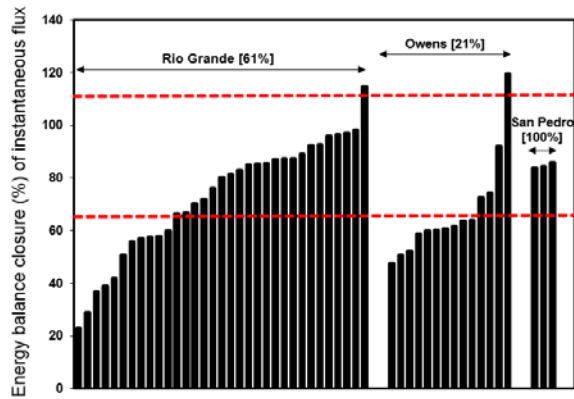
1957
1958
1959
1960
1961
1962
1963
1964
1965
1966
1967
1968
1969
1970
1971
1972
1973
1974
1975
1976

Formatted: Font: (Default) Times New Roman

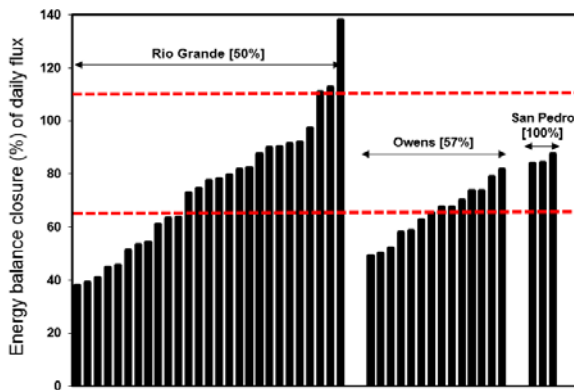
Formatted: Font: (Default) Times New Roman

Figure 1 Landsat7 scenes of the study areas in New Mexico, Arizona and California.
(PET: potential evapotranspiration; AAP: average annual precipitation)

1977
 1978
 1979
 1980
 1981



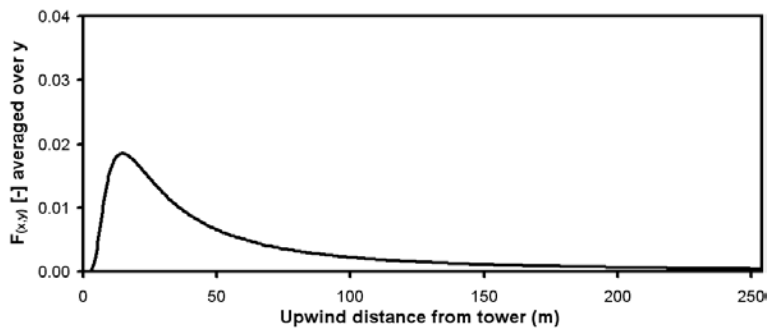
1982
 1983
 1984



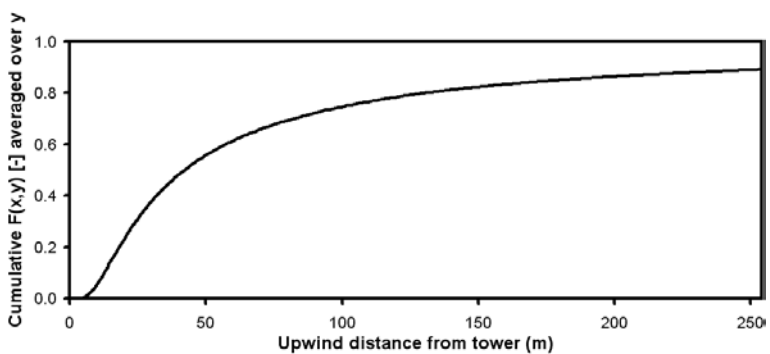
1985
 1986
 1987
 1988
 1989
 1990
 1991
 1992
 1993
 1994
 1995
 1996
 1997

Figure 2. Distribution of energy balance relative closure $(H+LE)/(R_n-G)$ of instantaneous (top panel) and total daily (bottom panel) fluxes from eddy covariance towers. Each 'bar' represents a satellite overpass day. The dotted lines show criteria of acceptable closure [65 and 110 %] and percentage of the data having acceptable closure is shown in bracket.

1998
1999
2000
2001
2002
2003



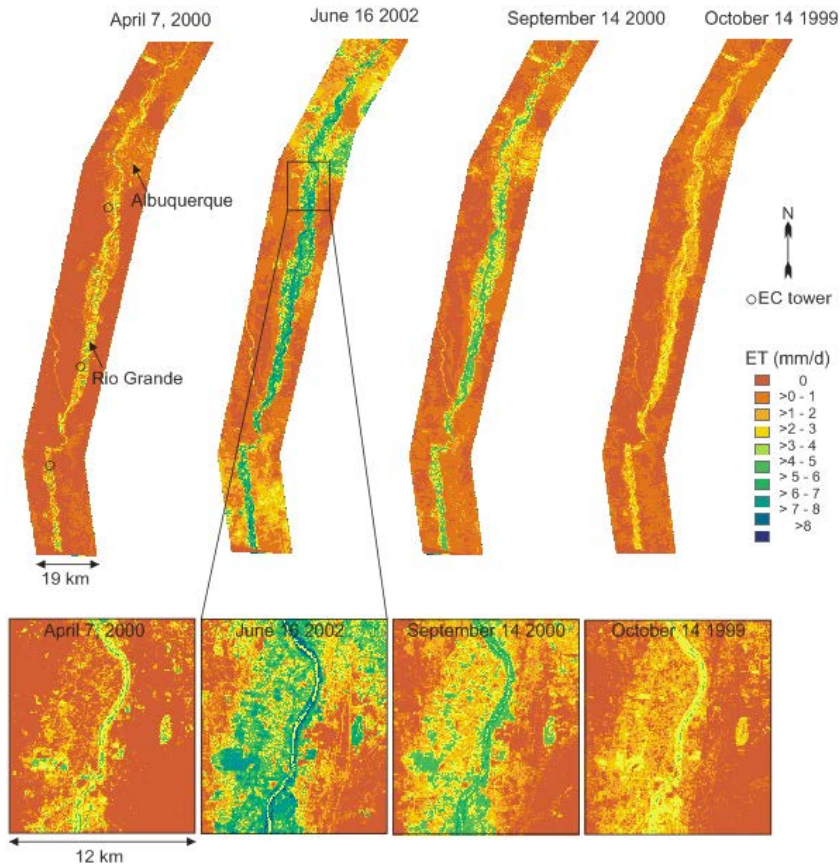
2004
2005
2006



2007
2008
2009
2010
2011
2012
2013
2014
2015
2016
2017
2018
2019
2020
2021
2022
2023

Figure 3. Footprint size and footprint intensity from the eddy covariance tower located at SEV (saltcedar) in Rio Grande on August 19, 2002 (10:40 am) (wind speed: 3.4 m/s, vegetation height: 4.9 m and sonic anemometer height from ground: 6.5 m).

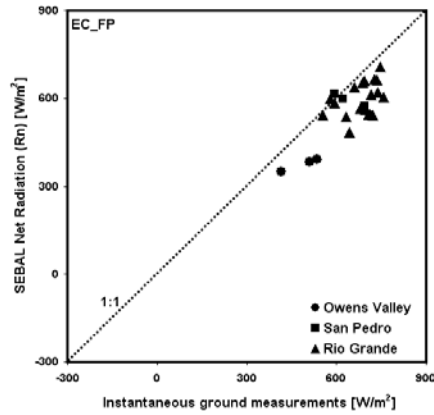
2024
2025
2026
2027



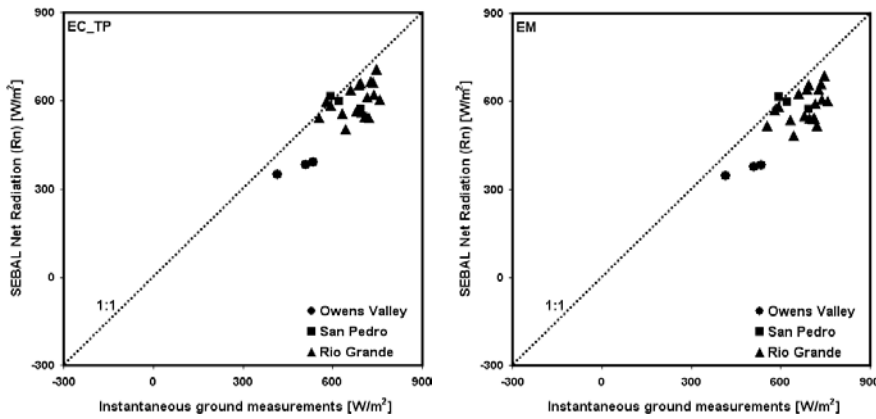
2028
2029
2030
2031
2032
2033
2034
2035
2036
2037
2038
2039
2040

Figure 4. SEBAL daily evapotranspiration (mm/d) maps along the Rio Grande in spring, summer and fall.

2041
2042
2043



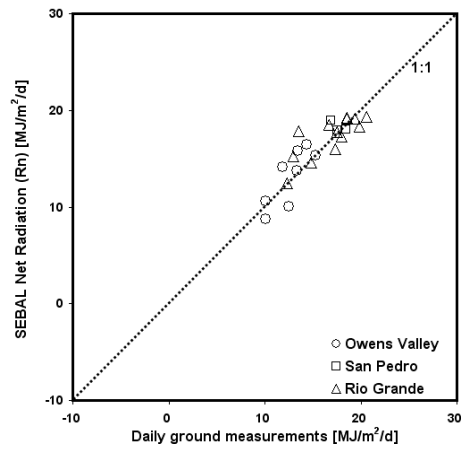
2044
2045
2046



2047
2048
2049
2050
2051
2052
2053
2054
2055
2056
2057
2058
2059
2060

Figure 5. Comparison of instantaneous net radiation (R_n) between net radiometer measurements and SEBAL estimates. (EC_FP (S1) method selected anchor pixels to match fluxes of the ground measured instantaneous LE (adjusted for closure error) at the satellite overpass and the footprint weight averaged SEBAL LE . EC_TP (S2) method selected anchor pixels to match fluxes of the ground measured instantaneous LE and the flux of the tower pixel. EM (S3) method selected the anchor pixels with the hydrogeological features of the landscape and micrometeorological considerations.

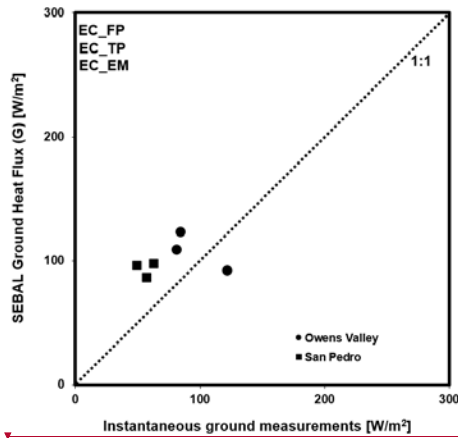
2061
2062
2063
2064
2065
2066
2067



2068
2069
2070
2071
2072
2073
2074
2075
2076
2077
2078
2079
2080
2081
2082
2083
2084
2085
2086
2087

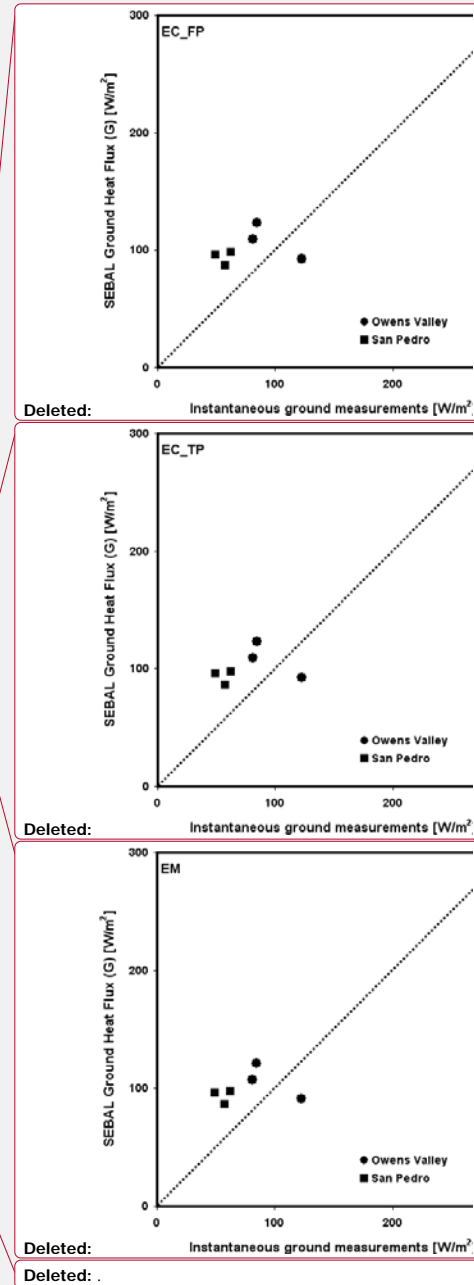
Figure 6. Comparison of daily net radiation (R_n) between net radiometer measurements and SEBAL estimates.

2088
2089
2090
2091
2092
2093

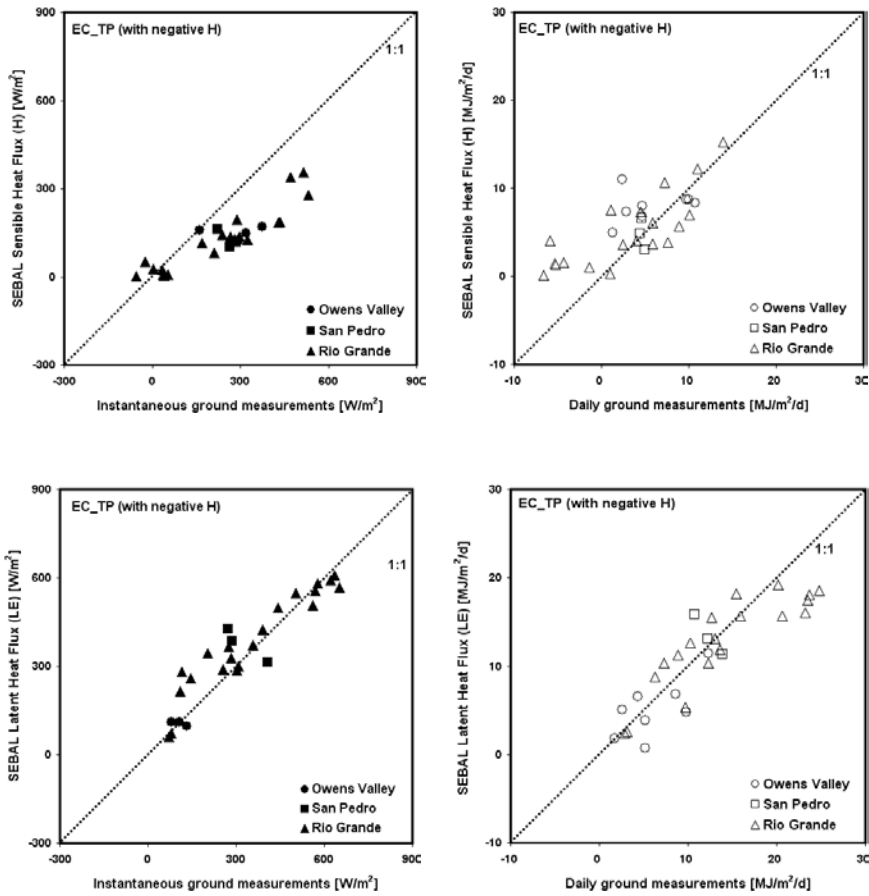


2094
2095
2096
2097
2098
2099
2100
2101
2102
2103
2104
2105
2106
2107
2108
2109
2110
2111
2112
2113
2114
2115
2116
2117

Figure 7. Comparison of instantaneous ground heat flux (G) between soil heat flux plate measurements and SEBAL estimates in Owens Valley and San Pedro Valley. EC_FP (S1), EC_TP (S2), and EM (S3) methods produced very similar SEBAL estimates.



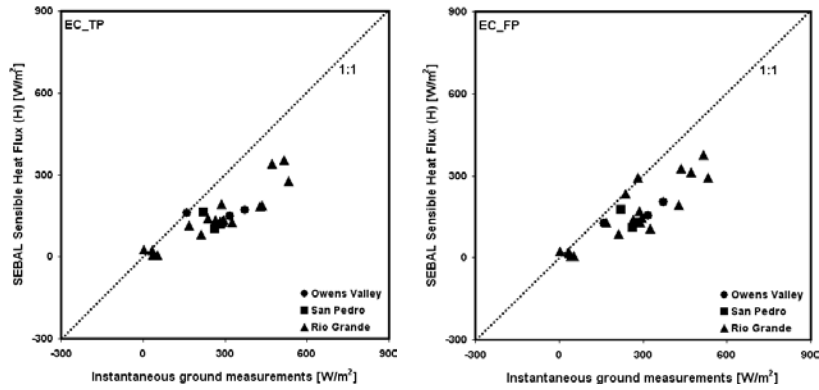
2122
2123
2124
2125



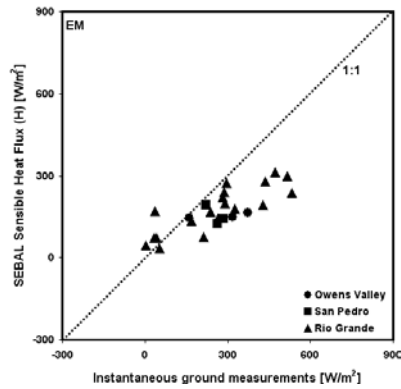
2126
2127
2128
2129

2130
2131
2132
2133
2134
2135
2136
2137
2138
2139
2140
2141

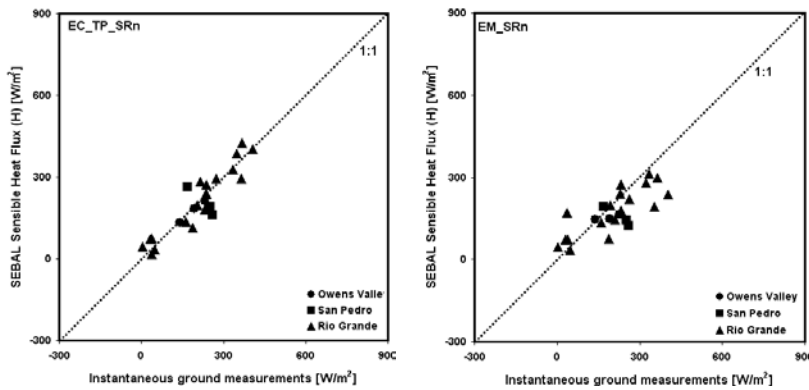
Figure 8. Comparison of sensible (H) and latent heat (LE) fluxes between adjusted eddy covariance tower measurements (with negative H data points) and SEBAL estimates from scenario S2 (EC_TP).



2142
2143

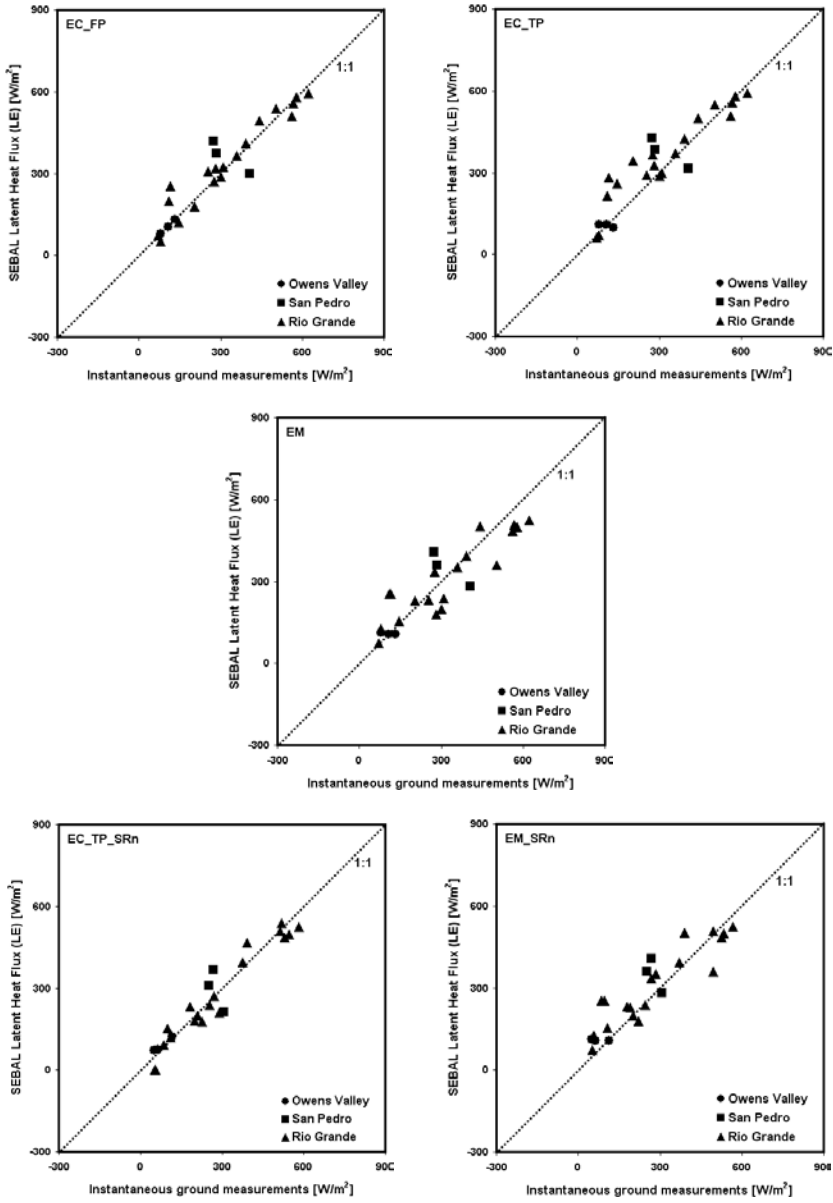


2144
2145



2146
2147
2148
2149

Figure 9. Comparison of instantaneous sensible heat flux (H) between adjusted eddy covariance tower measurements and SEBAL estimates for scenarios S1–S5.



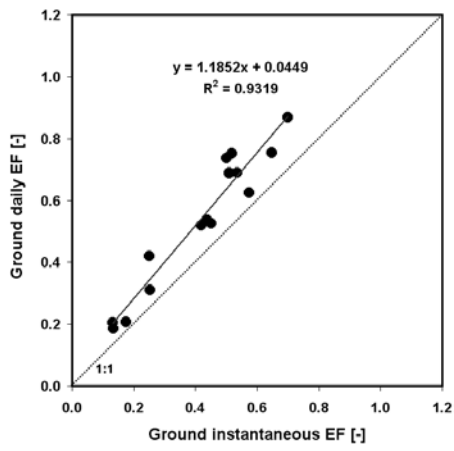
2150
2151

2152
2153

2154
2155
2156
2157
2158

Figure 10. Comparison of instantaneous latent heat flux (LE) between adjusted eddy covariance tower measurements and SEBAL estimates for scenarios S1–S5.

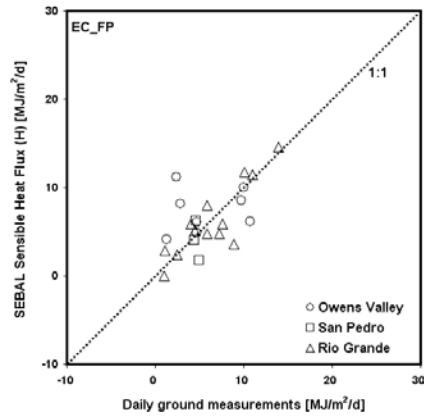
2159
2160
2161
2162
2163
2164
2165



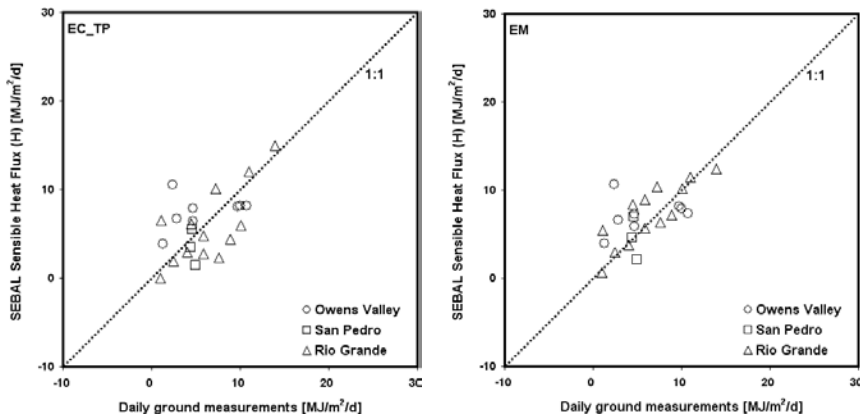
2166
2167
2168
2169
2170
2171
2172
2173
2174
2175
2176
2177
2178
2179
2180
2181
2182
2183
2184
2185

Figure 11. Comparison of satellite overpass instantaneous evaporative fraction (*EF*) with daytime average measured on the ground.

2186
2187
2188



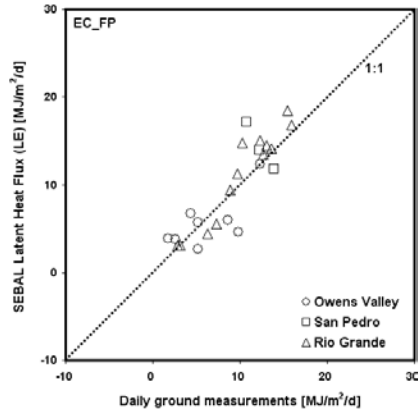
2189
2190
2191



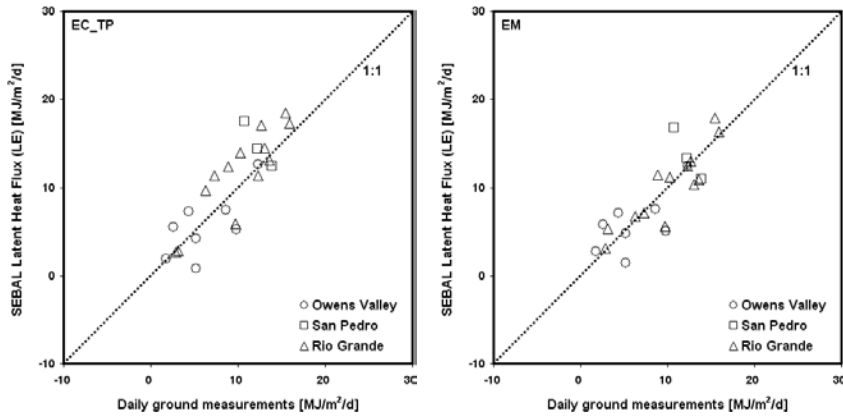
2192
2193
2194
2195
2196
2197
2198
2199
2200
2201
2202
2203
2204

Figure 12. Comparison of daily sensible heat flux (H) between adjusted eddy covariance tower measurements and SEBAL estimates. ($EF_{24} = 1.1 * EF_{inst}$)

2205
2206
2207



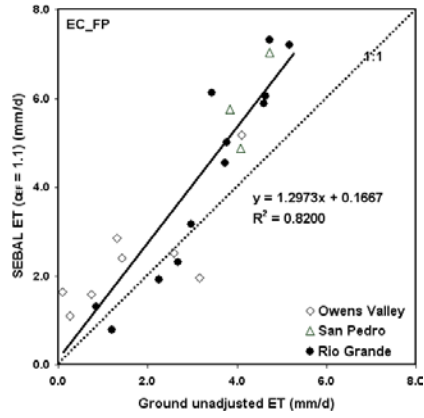
2208
2209
2210



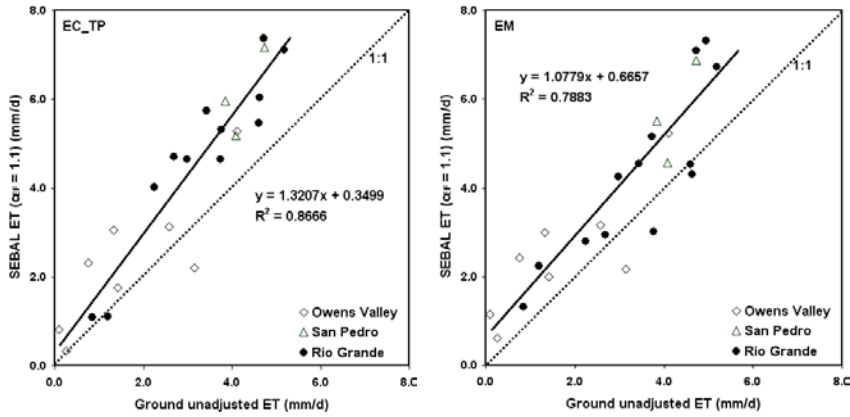
2211
2212
2213
2214
2215
2216
2217
2218
2219
2220
2221
2222
2223
2224

Figure 13. Comparison of daily latent heat flux (LE) between adjusted eddy covariance tower measurements and SEBAL estimates. ($EF_{24} = 1.1 * EF_{inst}$)

2225
2226
2227



2228
2229
2230



2231
2232
2233
2234
2235
2236
2237
2238
2239

2240 **Figure 14.** Comparison of ET rates determined from SEBAL with c_{EF} of 1.1 to eddy
2241 covariance ground measurements in riparian areas of the Rio Grande Valley (NM), San
2242 Pedro Valley (AZ), and Owens Valley (CA).